Geophysical Journal International

Geophys. J. Int. (2017) **211,** 349–377
Advance Access publication 2017 July 31
GJI Seismology

doi: 10.1093/gji/ggx305

Radial anisotropy of the North American upper mantle based on adjoint tomography with USArray

Hejun Zhu,[1] Dimitri Komatitsch[2] and Jeroen Tromp[3,4]

[1]*Department of Geosciences, The University of Texas at Dallas, TX,* 75080*, USA. E-mail: hejun.zhu@utdallas.edu*
[2]*Laboratory of Mechanics and Acoustics, CNRS, Aix Marseille University, Centrale Marseille, F-*13453 *Marseille, France*
[3]*Department of Geosciences, Princeton University, NJ* 08544*, USA*
[4]*Program in Applied & Computational Mathematics, Princeton University, NJ* 08544*, USA*

Accepted 2017 July 21. Received 2017 July 19; in original form 2016 September 28

SUMMARY

We use seismic data from USArray to image the upper mantle underneath the United States based on a so-called 'adjoint tomography', an iterative full waveform inversion technique. The inversion uses data from 180 regional earthquakes recorded by 4516 seismographic stations, resulting in 586 185 frequency-dependent measurements. Three-component short-period body waves and long-period surface waves are combined to simultaneously constrain deep and shallow structures. The transversely isotropic model US_{22} is the result of 22 pre-conditioned conjugate-gradient iterations. Approximate Hessian maps and point-spread function tests demonstrate good illumination of the study region and limited trade-offs among different model parameters. We observe a distinct wave-speed contrast between the stable eastern US and the tectonically active western US. This boundary is well correlated with the Rocky Mountain Front. Stable cratonic regions are characterized by fast anomalies down to 250–300 km, reflecting the thickness of the North American lithosphere. Several fast anomalies are observed beneath the North American lithosphere, suggesting the possibility of lithospheric delamination. Slow wave-speed channels are imaged beneath the lithosphere, which might indicate weak asthenosphere. Beneath the mantle transition zone of the central US, an elongated north–south fast anomaly is observed, which might be the ancient subducted Farallon slab. The tectonically active western US is dominated by prominent slow anomalies with magnitudes greater than −6 per cent down to approximately 250 km. No continuous lower to upper mantle upwellings are observed beneath Yellowstone. In addition, our results confirm previously observed differences between oceans and continents in the anisotropic parameter $\xi = (\beta_h/\beta_v)^2$. A slow wave-speed channel with $\xi > 1$ is imaged beneath the eastern Pacific at depths from 100 to 200 km, reflecting horizontal shear within the asthenosphere. Underneath continental areas, regions with $\xi > 1$ are imaged at shallower depths around 100 km. They are characterized by fast shear wave speeds, suggesting different origins of anisotropy underneath oceans and continents. The wave speed and anisotropic signatures of the western Atlantic are similar to continental areas in comparison with the eastern Pacific. Furthermore, we observe regions with $\xi < 1$ beneath the tectonically active western US at depths between 300 and 400 km, which might reflect vertical flows induced by subduction of the Farallon and Juan de Fuca Plates. Comparing US_{22} with several previous tomographic models, we observe relatively good correlations for long-wavelength features. However, there are still large discrepancies for small-scale features.

Key words: North America; Computational seismology; Seismic anisotropy; Seismic tomography.

1 INTRODUCTION

The surface geology of the Unites States (US) and its underlying mantle have been shaped over the past several hundred million years by interactions among four major plates, namely, the Pacific, North American, Farallon and Atlantic Plates (Coney *et al.* 1980; Hoffman 1988; Whitmeyer & Karlstrom 2007). The evolution of several small plates—the Juan de Fuca, Cocos and Caribbean Plates—also contributed to the complexities of this region. Fig. 1 shows the major geophysical provinces of the US. Over the past

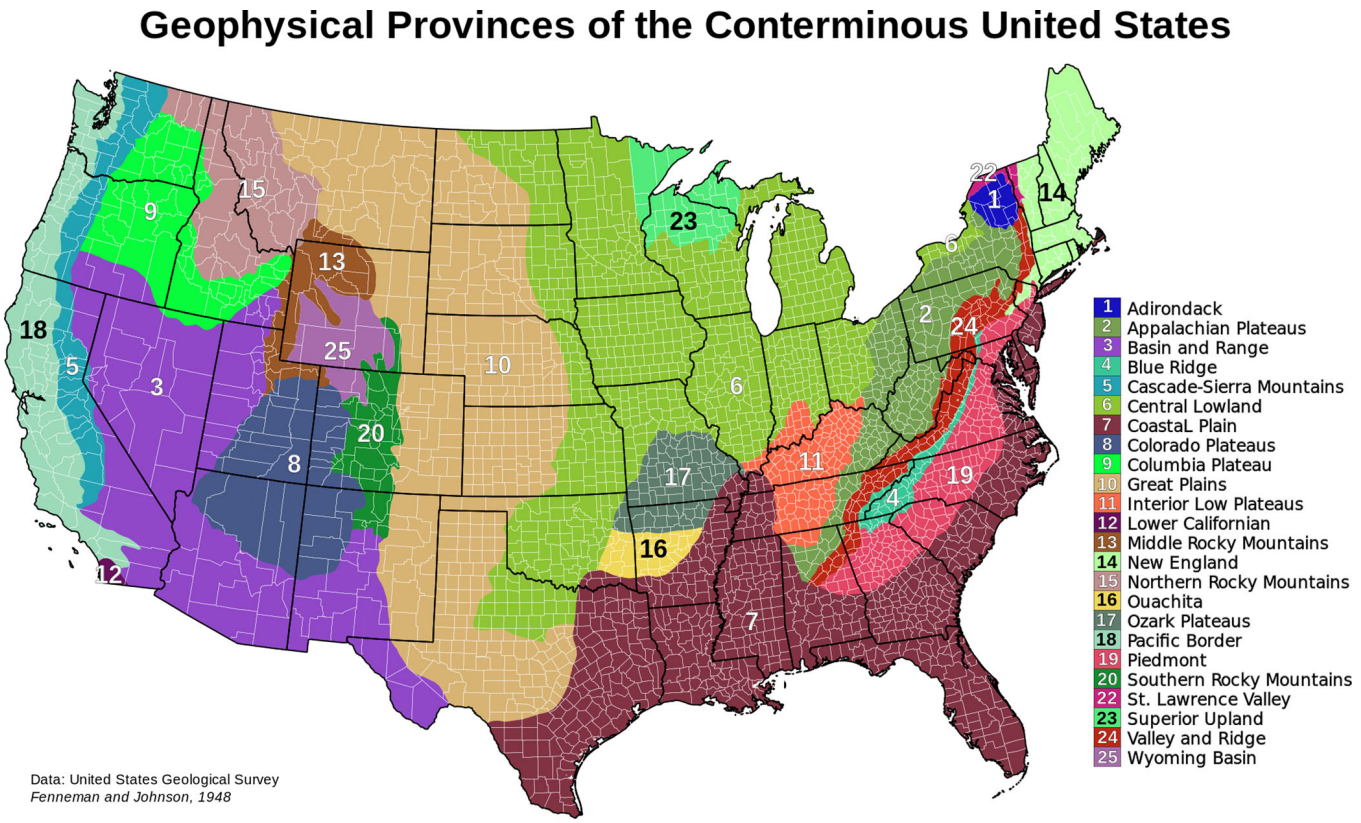

Figure 1. Major geophysical provinces of the US, adapted from https://commons.wikimedia.org/wiki/User:Kbh3rd.

several decades, geoscientists from different disciplines used a variety of techniques to investigate the geological, geochemical, and geophysical signatures of the US. Seismic tomography (Woodhouse & Dziewoński 1984; van der Hilst *et al.* 1991; Romanowicz 2003) provides a window into the Earth's interior, enabling us to map variations in wave speeds, anisotropy, and attenuation. These images are crucial for studying tectonic evolution, for example, by providing independent constraints for geodynamic modelling (Bunge & Grand 2000; Liu *et al.* 2008, 2010; Liu & Stegman 2012) and thermal structure inversions (Goes & van der Lee 2002).

Adjoint tomography is a high-resolution tomographic technique which combines high-quality seismic waveform records with accurate numerical modelling—such as the Spectral-Element Method (SEM; Komatitsch & Tromp 1999, 2002a,b) and the adjoint-state method (Tromp *et al.* 2005; Liu & Tromp 2006, 2008)—to map Earth's interior. It is closely related to the Full Waveform Inversion (FWI) method introduced by Tarantola (1984) and Lailly (1983) for mapping acoustic wave-speed variations at reservoir scales. The adjoint method is used to numerically compute misfit gradients, which are used to iteratively update seismic model parameters in order to fit observed and predicted measurements, such as least-squares waveform or phase/amplitude differences (Plessix 2006; Virieux & Operto 2009). Recently, adjoint tomography and FWI have been used to study the crustal structure of southern California (Chen *et al.* 2007; Tape *et al.* 2009, 2010), and the crustal and upper-mantle structure of Australia (Fichtner *et al.* 2009), Europe (Zhu *et al.* 2015; Fichtner & Villaseñor 2015), southeast Asia (Chen *et al.* 2015) and the entire globe (Bozdağ *et al.* 2016). Sensitivity kernels with respect to radially and azimuthally anisotropic parameters have been introduced for both body- and surface-wave measurements (Sieminski *et al.* 2007a,b). Recently, adjoint tomography has also been applied to constrain continental-scale variations in transverse isotropy (also referred to as radial anisotropy; Fichtner *et al.* 2010; Zhu *et al.* 2012), azimuthal anisotropy (Zhu & Tromp 2013), as well as anelastic attenuation (Zhu *et al.* 2013). In order to incorporate high-frequency body waves, a hybrid technique was developed by incorporating teleseismic wavefields from direction solution method in adjoint tomography (Monteiller *et al.* 2015; Wang *et al.* 2016). A detailed review of recent progress in adjoint tomography may be found in Liu & Gu (2012).

This study is the first attempt to determine a 3-D seismic model of the North American crust and upper mantle based on adjoint tomography and USArray data. We begin by reviewing previous US tomographic studies. We then describe our dataset and the methods used to construct model US_{22}. Point-spread functions (PSFs) are used to analyse resolution and trade-off between different model parameters. Next, we discuss the isotropic shear wave-speed structure of US_{22} and compare it with several available body- and surface-wave models. Finally, we present the radially anisotropic structure of US_{22} and compare it with two existing surface-wave models.

2 REVIEW OF PREVIOUS TOMOGRAPHIC STUDIES

2.1 Isotropic models

Since the 1970s, seismologists have used seismic tomography to study the US mantle. Based on body-wave arrival times, Romanowicz (1979) constructed the first 3-D upper-mantle model for the US, mapping a sharp contrast between the western and eastern US. Using *S*-wave traveltimes, Grand (1994) mapped shear wave-speed variations beneath North America and its surrounding areas. A sheet-like fast anomaly was observed from the bottom

of the transition zone into the deep mantle, which was interpreted as subducted lithosphere of the ancient Farallon Plate. This observation was confirmed later in a global *P* model (van der Hilst *et al.* 1997). By synthesizing these two *P* and *S* models, built using different techniques and data sets, Grand *et al.* (1997) found good correlation between wave-speed heterogeneities on both long and short lengthscales. For instance, fast anomalies mapped within the lower mantle suggested that slabs continue into the lower mantle and reach the core–mantle boundary. These tomographic models also provided independent constraints for geodynamical forward modelling (Bunge & Grand 2000) and backward reconstruction (Liu *et al.* 2008). The P & S models suggested low-angle subduction of the Farallon Plate during the Mesozoic, which was proposed previously based on the geochronology of igneous rocks in the western US (Coney & Reynolds 1977) and numerical simulations of the formation of the Rocky mountains (Bird 1988). Due to limited depth resolution and data coverage in global body-wave tomography, the US upper mantle remained relatively poorly constrained, which required the construction of regional tomographic models.

Before the deployment of USArray, several regional tomographic studies used seismic networks available at that time, such as NEIC, USNSN, GDSN, etc., to image US upper mantle structure. For instance, van der Lee & Nolet (1997b) applied partitioned waveform inversion (Nolet 1990) with fundamental/higher-mode Rayleigh waves to constrain upper-mantle shear wave-speed structure. Several fast anomalies observed within the upper mantle and transition zone were interpreted as fragments of the ancient Farallon slab (van der Lee & Nolet 1997a). This continental-scale tomographic study provided complementary information about the fate of the subducted Farallon slab. The thermal structure of the North American uppermost mantle was determined by Goes & van der Lee (2002) based on this tomographic model. Subsequently, this model was updated several times using better data coverage and different inversion strategies (van der Lee 2002; van der Lee & Frederiksen 2005; Bedle & van der Lee 2009). Combining surface-wave dispersion and gravity data, Godey *et al.* (2004) jointly determined shear wave speed and density heterogeneities, which were used to infer thermal and compositional variations underneath North America.

Over the past 10 yr, EarthScope deployed the USArray transportable array to cover the contiguous US in meridional swaths, starting in the west and concluding in the east. Its 70 km $\times$70 km grid spacing provides seismologists with unprecedented data coverage for probing crust and mantle heterogeneities. Earlier tomographic images have been significantly improved based on USArray data, first for the western US and subsequently, as the array moved eastward, beneath the central and eastern US. For instance, Sigloch *et al.* (2008) used multi-frequency body-wave tomography to build a *P* wave-speed model for the US down to approximately 1800 km. They observed interesting fast anomalies within the lower mantle beneath the central and eastern US, which were interpreted as a consequence of a two-stage subduction history of the Farallon Plate over the past 50 million years. This model was further analysed by Sigloch (2011) using 3-D visualization tools. A similar inversion approach was adopted by Tian *et al.* (2011) to construct 3-D shear wave-speed and attenuation models of the US using a combination of *SH* and Love waves. Taking into account frequency-dependent sensitivity kernels and the USArray deployment in the western US, Schmandt & Humphreys (2010) built *P* and *S* wave-speed models for the western US upper mantle. Compared to previous global-scale tomographic images, they observed much more complicated small-scale heterogeneities in the western US and high Vp/Vs ratios beneath Yellowstone and the Snake River Plain. Recently, this model was extended to the East Coast using eastern USArray data, making crustal corrections based on the latest ambient noise models (Schmandt & Lin 2014). Considering the different depth sensitivities of body and surface waves, Obrebski *et al.* (2011) and Porritt *et al.* (2014) jointly inverted body-wave traveltimes and surface-waves phase speeds in order to simultaneously constrain deep and shallow structures. Burdick *et al.* (2013) published several US models based on P-wave traveltime tomography. They documented improvements in resolution due to progressive contributions of USArray data. Recently, several models based on a waveform inversion framework have been proposed by incorporating USArray data (Schaeffer & Lebedev 2014; Yuan *et al.* 2014). Combining tomographic models with other seismic observations, such as SKS measurements and Ps/Sp receiver functions, several interesting small-scale mantle convection features were suggested, such as a lithospheric drip beneath the Great Basin (West *et al.* 2009) and delamination beneath the Colorado Plateau (Levander *et al.* 2011).

The dense coverage and high data quality of USArray also provided opportunities for developing new imaging and array processing techniques, such as ambient noise tomography (Shapiro *et al.* 2005; Bensen *et al.* 2007) and seismic gradiometry (Langston 2007a,b,c; Liu & Holt 2015). To date, ambient noise tomography has made significant contributions to studies of the US crust and uppermost mantle (Moschetti *et al.* 2010; Lin *et al.* 2008, 2009, 2011; Lin & Ritzwoller 2011). Considering the complementary sensitivities of surface waves and receiver functions to wave-speed variations and impedance contrasts (Bodin *et al.* 2012; Shen *et al.* 2013a; Calò *et al.* 2016), Shen *et al.* (2013b) combined these two data sets to better constrain shear wave-speed variations within the crust and uppermost mantle. Besides these large-scale tomographic studies, several local surveys based on temporary seismic arrays, such as the CD-ROM experiment (Levander *et al.* 2005; Yuan & Dueker 2005), also provided important constraints on the tectonic evolution of the US. Improved receiver function analysis has also been used to image the United States (Tauzin *et al.* 2013, 2016).

2.2 Anisotropic models

Seismic anisotropy is ubiquitous within Earth's interior. Some minerals and rocks within the crust and upper mantle are intrinsically anisotropic, such as mica, amphibole, olivine, and orthopyroxene. Lattice-Preferred Orientation (LPO; Nicolas & Christensen 1987; Zhang & Karato 1995; Jung & Karato 2001) and Shape-Preferred Orientation (SPO; Backus 1962) are the two most important mechanisms for seismic anisotropy within the crust and upper mantle. Over the past several decades, two relatively simple types of anisotropy, namely, radial and azimuthal anisotropy, have been extensively studied (Hess 1964; Backus 1965; Smith & Dahlen 1973; Montagner & Nataf 1986). In order to constrain anisotropy, several seismic tools have been developed, such as SKS splitting measurements (Silver & Chan 1991; Silver 1996), surface-wave tomography (Montagner & Tanimoto 1991; Simons *et al.* 2002; Debayle *et al.* 2005) and waveform inversion (Fichtner *et al.* 2010; Zhu *et al.* 2012; Zhu & Tromp 2013). Seismic anisotropy provides valuable complementary information about the Earth's dynamics and material properties (Vinnik *et al.* 1992; Park & Levin 2002; Long & Silver 2008).

Radial anisotropy is a type of transverse isotropy with a radial axis of symmetry (Thomsen 1986). The well-known 'Rayleigh-Love discrepancy' has been discussed theoretically (Anderson 1961) and has

been observed in various locations (Shapiro *et al.* 2004; Moschetti *et al.* 2010). Basically, one cannot simultaneously fit Rayleigh- and Love-wave dispersion curves using isotropic wave speeds if the medium is radially anisotropic. In order to explain Rayleigh and Love data as well as normal modes, radial anisotropy was introduced in the Preliminary Reference Earth Model (PREM; Dziewoński & Anderson 1981) from the bottom of the Moho to a depth of 220 km. Early tomographic studies have shown that lateral variations in radial anisotropy may be as significant as shear wave-speed variations at depths shallower than 250 km (Montagner & Tanimoto 1991; Ekström & Dziewoński 1998), suggesting the importance of both thermal variations and mantle flow within the lithosphere and asthenosphere. Taking into account radial anisotropy reconciled discrepancies among different tomographic models, for instance, beneath stable shields from 200 to 400 km (Gung *et al.* 2003) and beneath the Pacific Plate at shallow depths (Ekström & Dziewoński 1998).

Over the past several decades, radially and azimuthally anisotropic structures within the crust and upper mantle of the US have been studied using different techniques. For the western US, Moschetti *et al.* (2010) used surface-wave dispersion curves measured from ambient noise cross-correlations to map radial anisotropy within the crust and uppermost mantle. In order to explain both Rayleigh and Love dispersion curves, they introduced radial anisotropy within the lower crust beneath the Basin and Range, which was interpreted as a consequence of significant Cenozoic extension in this area. Furthermore, Lin *et al.* (2011) mapped complicated azimuthally anisotropic features in the crust and uppermost mantle beneath the western US using Rayleigh-wave ambient noise measurements. Combining surface-wave waveforms and SKS measurements, Marone *et al.* (2007) constructed 3-D radially and azimuthally anisotropic models for North America. Their azimuthally anisotropic results show a depth dependence of fast-axis directions (Marone & Romanowicz 2007). Yuan & Romanowicz (2010) and Yuan *et al.* (2011) improved these studies and observed two anisotropic layers within the cratonic lithosphere beneath North America, which were interpreted as chemical and thermal boundary layers within the continental lithosphere. Based on Rayleigh and Love wave dispersion, Nettles & Dziewoński (2008) inverted for radial anisotropy on a global scale with a focus on the North American continent. They observed significant differences in radial anisotropy beneath oceans and continents. For instance, channels with large radial anisotropy were observed at depths between 100 and 200 km beneath oceans. However, this feature was imaged at shallower depths beneath continents. In contrast to isotropic shear wave-speed variations, no prominent age-dependent radial anisotropy was observed beneath the Pacific Plate, suggesting different mechanisms for shear wave-speed variations and radial anisotropy beneath oceans.

3 DATA AND METHOD

3.1 Earthquakes and stations

In this study, we use 180 earthquakes to illuminate the North American continent. Their distribution is shown in Fig. 2. Most earthquakes occurred along major plate boundaries, for instance, the North Atlantic Ridge and boundaries around the Caribbean and Cocos Plates. Statistical information about the source parameters is presented in Fig. 3. The events occurred from 2003 to 2014, covering most of the duration of USArray. Their moment magnitude (M_w) ranges from 4.5 to 6.5 with a mean value around 5.5. The depth of most earthquakes is shallower than 30 km, except for a few events with a depth greater than 100 km. The half-duration of the source mechanisms for these earthquakes is 1–2 s. The initial source parameters of these earthquakes are collected from the global CMT solutions (www.globalcmt.org).

We used data from 4516 seismographic stations in this study. Their distribution is shown in Fig. 2. Of these stations, 1579 stations come from USArray. Other arrays deployed between 2003 and 2014 are also incorporated in our dataset. Major network contributions include CN (62 stations), AK (64), US (70), UW (74), XI (76), XN (80), PB (83), XQ (87), UU (91), CI (102), XE (106), XC (118), TO (142) and ZH (170). Due to the configuration of USArray, most stations correspond to less than 40 earthquakes in our data set.

The depth range in the inversion extends from Earth's surface to 1000 km. Lateral boundaries of the model are shown in Fig. 2. An absorbing boundary condition is applied to avoid reflections from artificial boundaries (Stacey 1988), and the starting model is fixed for the outside model.

3.2 Approximate Hessian

Following Zhu *et al.* (2015), we present the approximate diagonal of the Hessian in Fig. 4. It is computed by correlating forward and adjoint acceleration wavefields (Luo *et al.* 2013), and is a good proxy for ray density. Limited-memory Broyden–Fletcher–Goldfarb–Shanno method (L-BFGS; Matthies & Strang 1979; Nocedal 1980) might be a better approximation which has been explored by Monteiller *et al.* (2015) and Modrak & Tromp (2016). Due to the configuration of earthquakes and stations in Fig. 2, at depths shallower than 400 km we have good illumination of the entire region, including Cascadia and the Caribbean. Below 400 km, illumination of the eastern US, the Caribbean, and Cascadia starts to degrade. At depths greater than 700 km, we only have good coverage in the central US.

3.3 Source inversions

Before the structural inversion, we perform source inversions in order to correct possible biases in the global CMT solutions, as reported in Zhu *et al.* (2015). We use waveform data from global seismic networks to constrain latitude, longitude, and depth, as well as the six components of the moment tensor. The distribution of global stations used to constrain the source parameters is shown in Fig. 5(b) and provides good azimuthal coverage. Global model S362ANI (Kustowski *et al.* 2008) is used for the source inversions. Body waves with periods between 30 and 80 s and surface waves with periods between 80 and 120 s are combined to constrain the source parameters. Following Liu *et al.* (2004), during the source inversion we numerically compute Green's functions and sensitivity kernels with respect to the nine source parameters. Time-shifted waveform differences are used in the misfit function. Details about weighting terms associated with azimuths, distances, and phases are discussed in Liu *et al.* (2004) and Zhu *et al.* (2015). Similar to observations made by Zhu *et al.* (2015), there are no systematic changes in latitude, longitude, and moment tensor. However, we do find systematic changes in depth. In Fig. 5(a), the depth of most earthquakes after source inversion is approximately 5 km shallower than the corresponding global CMT solutions, especially for events beneath the North Atlantic Ridge. Fig. 5(c) compares the original CMT depth with the depth after inversion. Since the minimum depth allowed in the global CMT solutions is ∼12 km, in our inversion these events are often located shallower. From the histogram of

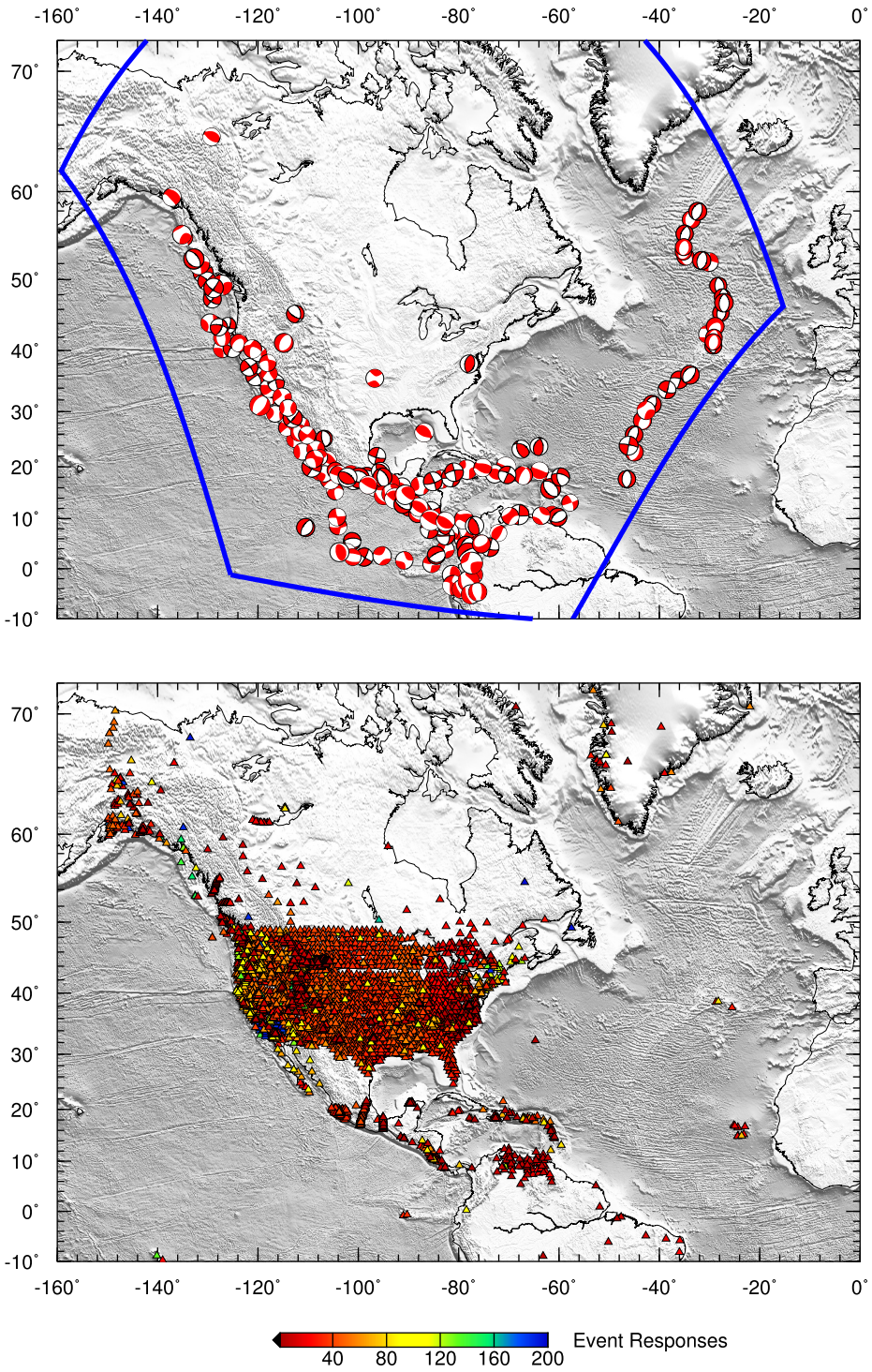

Figure 2. Earthquakes and stations used in the inversion. The top panel shows the distribution of 180 earthquakes. Initial source parameters of these earthquakes are gathered from the global CMT program (www.globalcmt.org). The blue lines denote the SEM simulation region. The bottom panel shows the seismic stations used in this study. The colour of each station indicates the number of earthquakes for which it contributed data.

depths shown in Fig. 5(d), we see that the depth of some events is not changed significantly. Besides these unchanged events, there is a Gaussian distribution with a mean depth change of ~ -5 km, indicating that the new depths are approximately 5 km shallower than the original global CMT solutions. One possible reason for this depth bias might come from 3-D crustal approximations used in the global CMT inversion (Hjörleifsdóttir & Ekström 2010). Another possible reason is that no mantle waves with periods greater than 135 s (Dziewoński & Woodhouse 1983; Ekström *et al.* 2012) are used in our source inversions, which might result in biased depth estimates (Abercrombie & Ekström 2001).

3.4 Starting model US_{00}

Adjoint tomography involves a nonlinear inverse problem, and therefore a good starting model is crucial for its convergence. If

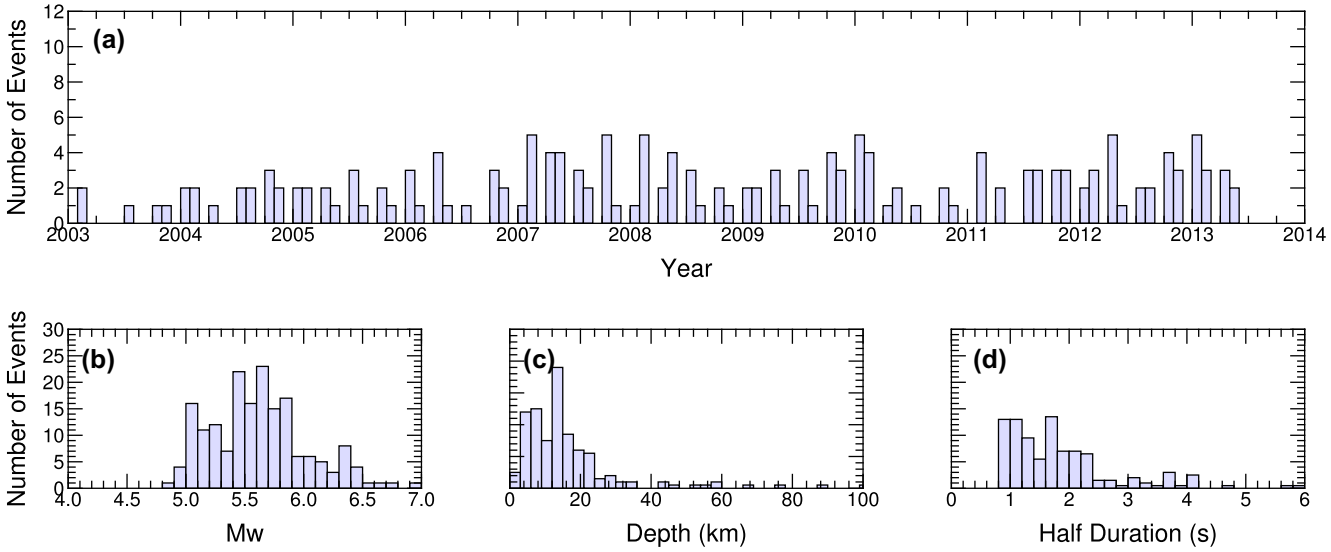

Figure 3. Earthquake source parameters. (a) Distribution of origin times for the earthquakes in Fig. 2. (b)–(d) Histograms of moment magnitudes, depths and half durations, respectively.

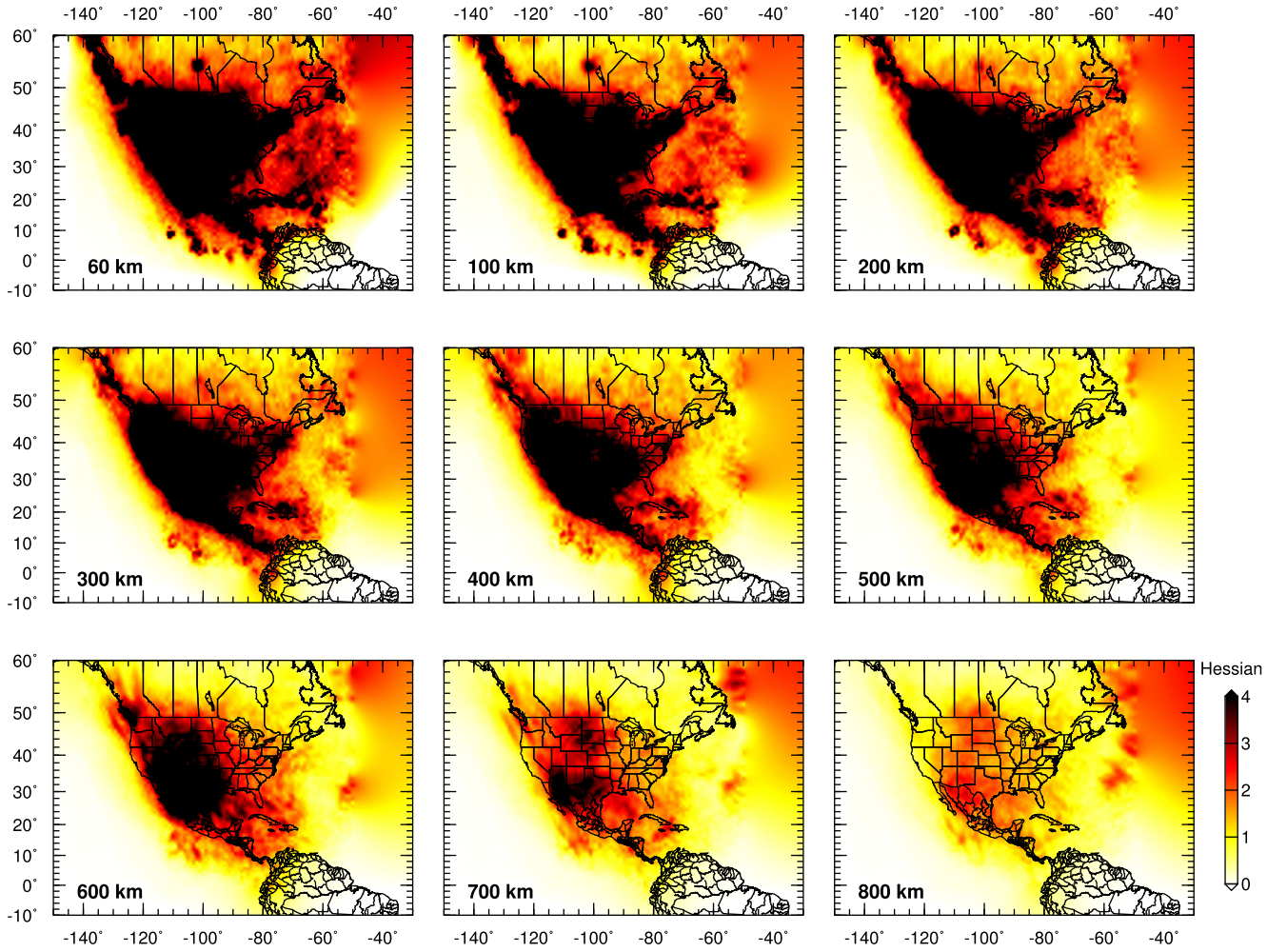

Figure 4. Horizontal cross-sections of the approximate Hessian at depths ranging from 60 to 800 km. Warm colours indicate relatively good illumination.

the starting model is far away from the global minimum and the misfit function involves numerous local minima, iterative inversion cannot guarantee convergence towards the correct solution (Gauthier *et al.* 1986; Zhu & Fomel 2016). In this study, the starting model US_{00} is built by combining crustal model CRUST2.0 (Bassin *et al.* 2000) and mantle model S362ANI (Kustowski *et al.* 2008). The spectral-element mesh is stretched to honour Moho variations in CRUST2.0 (Tromp *et al.* 2010). Supporting Information Fig. S1

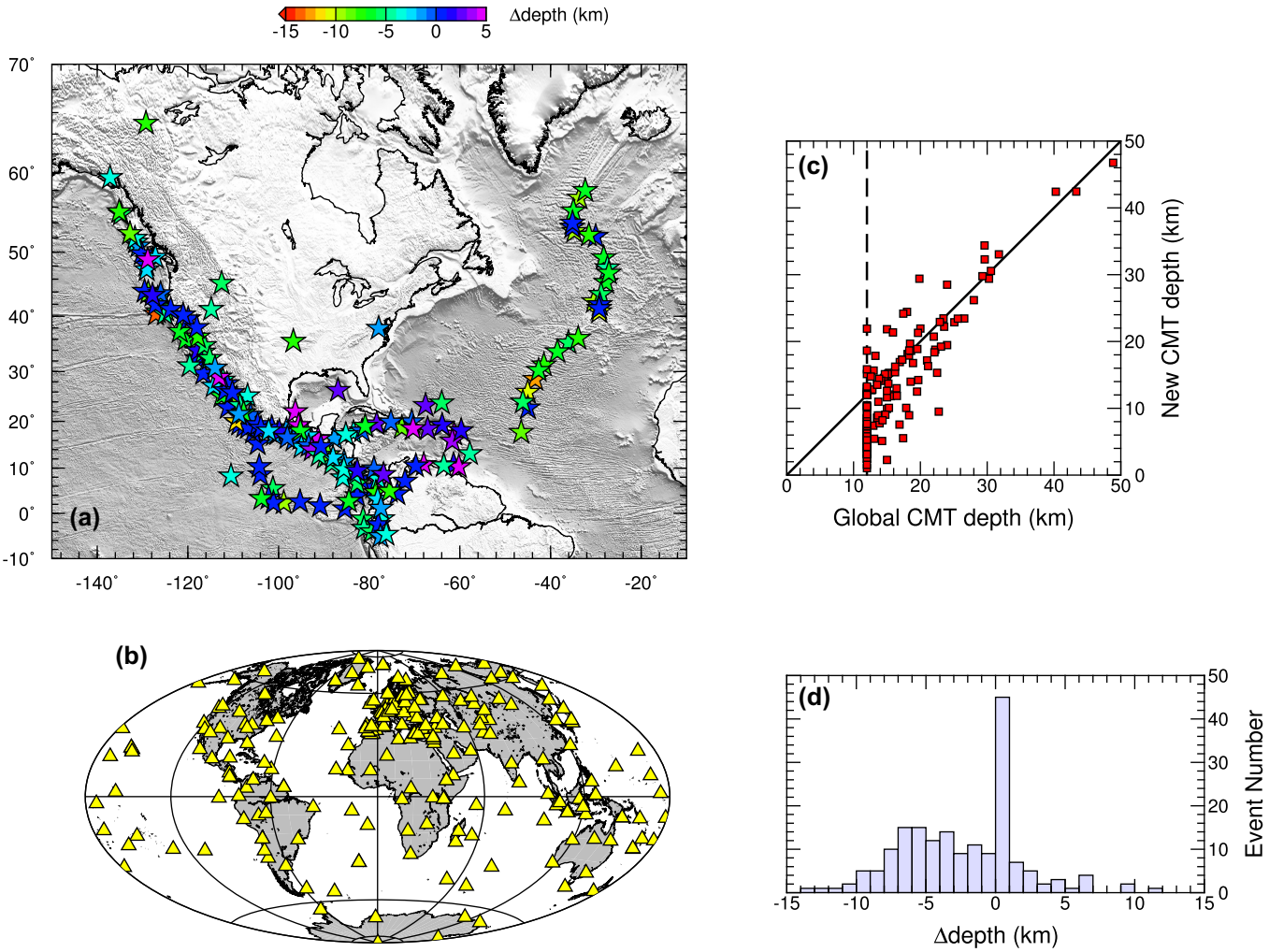

Figure 5. Depth changes following the 3-D source inversions. (a) Map view of depth changes after 3-D source inversion. (b) Distribution of stations used in the source inversion. (c) New depths compared to the original CMT solutions. (d) Histogram of depth changes, that is, differences between the new and original depths.

presents relative perturbations in the Voigt-averaged isotropic shear wave speed, $\beta = \sqrt{(2\beta_v^2 + \beta_h^2)/3}$, and the radially anisotropic parameter, $\xi = (\beta_h/\beta_v)^2$, for US_{00} from 50 to 300 km. Since S362ANI is a global shear wave-speed model, on this continental-scale it only involves relatively long-wavelength heterogeneities. For instance, at shallow depths (<300 km), it involves a significant wave-speed contrast between the fast eastern US and the slow western US. The magnitude of these anomalies is relatively large (>6 per cent) in comparison with other regions in the world. Below 300 km, the magnitude of wave-speed perturbations reduces significantly to around 2 per cent. The Farallon slab is not very clear in US_{00} in comparison with early body-wave traveltime images (Grand 1994; van der Hilst *et al.* 1997) because S362ANI was designed to constrain long-wavelength variations. In S362ANI, radial anisotropy is allowed from the bottom of the Moho to around 300 km (Kustowski *et al.* 2008). From 100 to 200 km, the studied region is dominated by long-wavelength structure with a radially anisotropic parameter $\xi > 1$. The magnitude of radial anisotropy reduces dramatically at depths greater than 200–250 km. Considering the possibility of anisotropy within the mantle transition zone (Trampert & Van Heijst 2002), radial anisotropy is allowed in our inversion from the bottom of the Moho to the bottom of the mantle transition zone. Although crustal anisotropy, especially within the lower crust, might be an important proxy for studying shear flow and material properties at shallower depths (Shapiro *et al.* 2004; Moschetti *et al.* 2010), it is not considered in the current inversion. 1-D reference model STW105 (Kustowski *et al.* 2008) is used to calculate relative perturbations in shear wave speeds in this paper.

3.5 Model parametrization

Radial anisotropy may be characterized in terms of the five Love parameters A, C, L, N, and F (Love 1927). Because phase measurements are the main focus of the current inversion, we prefer to use a wave-speed parametrization instead. The model parameters considered in the inversion include the speed of horizontally travelling and vertically polarized shear waves (β_v), the speed of horizontally travelling and horizontally polarized shear waves (β_h), the bulk sound speed (c), and the dimensionless parameter η, which determines wave speeds at oblique propagation directions. We cannot resolve P-wave anisotropy with the current data set, which is why we opt to invert for the isotropic bulk sound speed; consequently the number of model parameters is reduced from 5 (A, C, L, N, and F) to 4 (β_v, β_h, c, and η). Sensitivity kernels with respect to these four model parameters are used in the inversion (Sieminski *et al.* 2007a,b; Zhu *et al.* 2015). Due to the insensitivity of

traveltimes to density variations, in this study we use a constant scaling relation between relative perturbations in density and relative perturbations in isotropic shear wave speed ($\delta \ln\rho = 0.33\,\delta \ln\beta$) to update the density model.

3.6 Data misfit

At this stage we only focus on phase differences between observations and simulations in order to constrain shear wave-speed structure. Synthetic seismograms and Fréchet derivatives are calculated based on the spectral-element solver SPECFEM3D_GLOBE (Komatitsch & Tromp 2002a,b), accommodating effects due to rotation, self-gravitation, the oceans, ellipticity & topography. Full attenuation in forward and adjoint simulations is taken into account based on a recently developed parsimonious storage technique (Komatitsch *et al.* 2016). A multitaper technique (Park *et al.* 1987; Simons *et al.* 2000; Zhou *et al.* 2004) is used to measure phase differences between simulated and observed seismograms. This approach allows us to quantify frequency-dependent phase differences and estimate standard deviations associated with each measurement, which can be integrated into the definition of the data misfit function. Three-component seismograms are used in this study. FLEXWIN (Maggi *et al.* 2009), an automatic window selection package, is used to select measurement windows by comparing observations with predications. We combine long-period surface waves and short-period body waves to simultaneously constrain deep and shallow structures. This strategy enables us to bridge the gap between body- and surface-wave tomography. Earlier studies, such as Ritsema *et al.* (1999), also used multiple data sets, including body-waves, surface-waves and normal mode observations. Using a similar strategy, recent work by Moulik & Ekström (2014, 2016) jointly modelled multiple data sets with long-period waveforms. Our total misfit function involves six contributions: Rayleigh waves on vertical and radial components, Love waves on transverse components, *P–SV* waves on vertical and radial components, and *SH* waves on transverse components.

In order to mitigate cycle skipping (Virieux & Operto 2009), we adopt a multiscale inversion strategy originally developed in FWI (Bunks *et al.* 1995; Sirgue & Pratt 2004). We start with long-period signals to first constrain long-wavelength structures. As the model and its predictions improve, we gradually incorporate shorter-period signals to constrain smaller-scale features. For instance, from the first to the fifth iteration we used a 15–50 s body-wave bandpass filter, while for subsequent iterations we switched to a 15–40 s bandpass. For surface waves we use four frequency bands, namely, 50–150 s, 40–150 s, 30–100 s, and 25–100 s. Each time increase the frequency band, there is a slight increase in data misfit. The reason we use a 100 s—rather than a 150 s—cut-off period is that the number of measurements for radial and transverse components diminishes at the longer-period cut-off. Fig. 6 shows the evolution of the total data misfit as well as its six contributions. In each category the misfit is gradually reduced over 22 iterations, as is the total misfit. Different weighting terms can be built into the misfit function in order to balance the six contributions. Since their magnitudes are relatively balanced in our inversion (Fig. 6), we do not add extra weighting terms in the total data misfit.

Fig. 7 compares histograms of phase measurements between the starting model US_{00} and the current model US_{22}. All six contributions to the total data misfit are presented. The mean phase measurements of all six contributions are shifted towards zero for US_{22} in comparison with US_{00}. Standard deviations for the new model are reduced compared to the starting model, demonstrating that US_{22} is capable of explaining both long-period surface waves and short-period body waves. Meanwhile, the number of phase measurements increases from 460 539 to 586 185, because more windows are selected for inversion as the model improves.

3.7 Point-spread function tests

Because of the computational cost and model dimensionality of adjoint tomography and FWI, quantifying uncertainty or resolution remains a challenge. To date, several procedures have been proposed to tackle this problem. For instance, Fichtner & van Leeuwen (2015) used random sampling to estimate the direction and position-orientated resolution of FWI. Bui-Thanh *et al.* (2013) and Zhu *et al.* (2016) formulated the problem in a Bayesian inference framework, and analysed posterior covariance based on a randomized SVD algorithm. Fichtner & Trampert (2011) and Zhu *et al.* (2015) used a finite-difference approximation to compute the PSFs, that is, the action of the Hessian on an impulsive model perturbation. These PSFs can be used to evaluate resolution and trade-off between different model parameters. Here, we follow this procedure to analyse the resolution of US_{22}, with a particular focus on trade-off between vertically and horizontally polarized shear wave speeds.

First, several Gaussian anomalies with a maximum amplitude perturbation of 2 per cent are used to perturb model US_{22} at a depth of 200 km. In order to analyse the trade-off between vertically and horizontally polarized shear wave speeds, we only perturb β_v and leave β_h unchanged. The left panel in Fig. 8 shows the locations of these input Gaussian anomalies. Next, we evaluate gradients with respect to the perturbed models. Using the differences between the current and new gradients, we obtain PSFs with respect to vertically and horizontally polarized shear wave speeds, as shown in the middle and right panels in Fig. 8. Resolution is relatively good for the western US, Texas, and the western Atlantic. However, a relative small horizontal shift in the PSF is observed near the US-Canada border. Smearing in the eastern US is relatively large. Overall, trade-off between β_v and β_h is relatively weak at this shallow depth, suggesting that the estimates of radial anisotropy in US_{22} are relatively robust at 200 km. Next, we use two Gaussian anomalies to assess resolution in the central and eastern US at a depth of 500 km (Fig. 9). Similar to Fig. 8, trade-off between β_v and β_h is relatively weak at this depth.

4 ISOTROPIC SHEAR WAVE-SPEED MODEL

4.1 Map views of US_{22}

In Fig. 10 we present the isotropic shear wave-speed structure of model US_{22} at depths ranging from 80 km to 800 km. At depths shallower than 200 km, similar to the starting model, we observe large wave-speed perturbations with magnitudes greater than 6 per cent, which suggest a non-thermal origin (Jackson & Faul 2010; Dalton & Faul 2010). These pronounced anomalies are well correlated with geological provinces. For instance, we observe a distinct wave-speed contrast between the stable eastern US and the tectonically active western US, which is consistent with previous studies (Romanowicz 1979; Grand 1994; van der Lee & Nolet 1997a). This wave-speed contrast is well correlated with the Rocky Mountain Front. At depths shallower than 100 km, the Snake River Plain is imaged as a prominent slow anomaly. Fast anomalies are observed

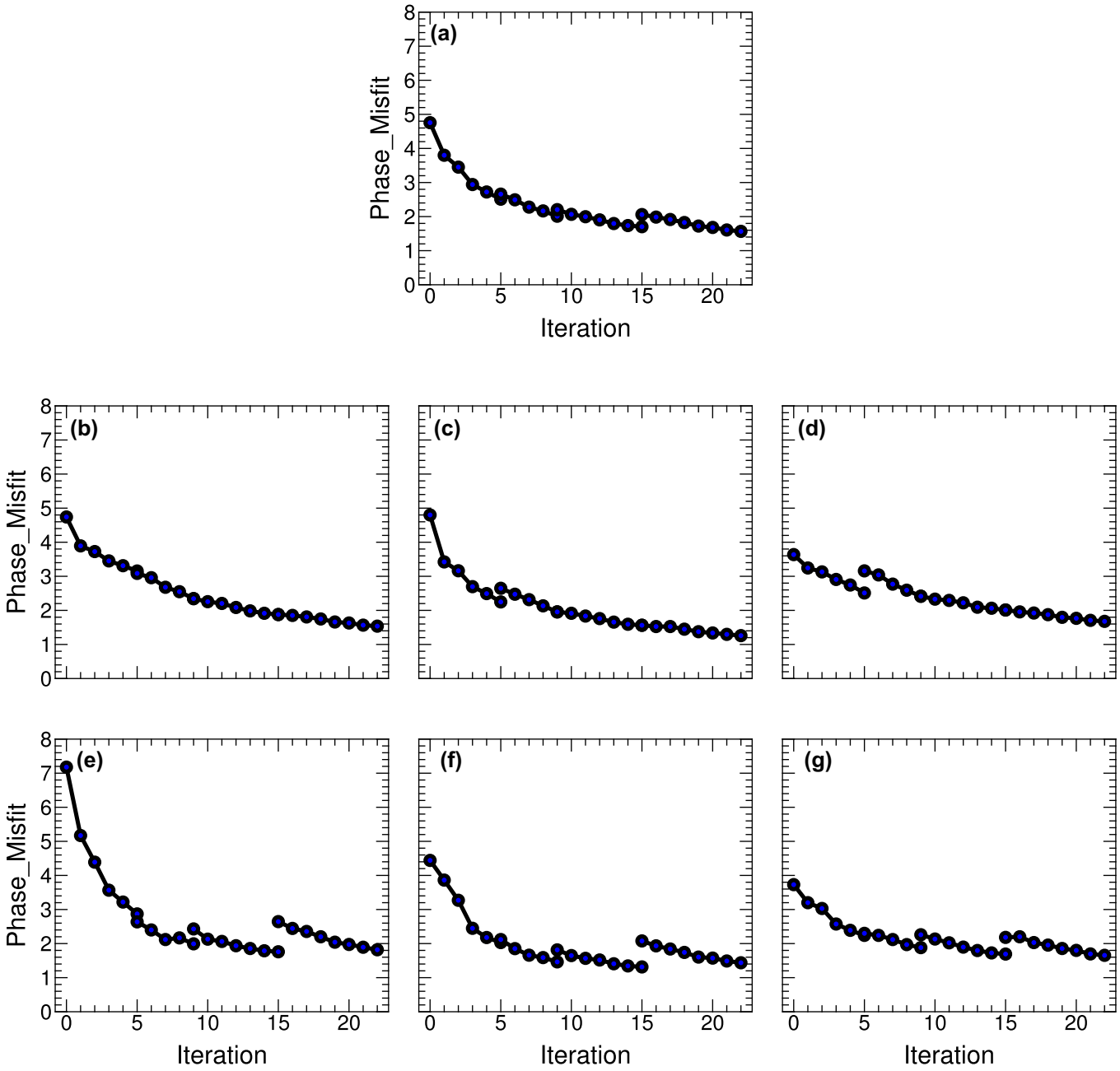

Figure 6. Evolution of the data misfit as a function of the iteration number. (a) Evolution of the total data misfit. (b)–(d) Evolution of the data misfits for vertical, radial and transverse components body waves, respectively. (e)–(g) Evolution of the data misfits for vertical, radial, and transverse components surface waves, respectively.

down to 300 km beneath cratonic areas, suggesting a relatively thick North American lithosphere (Gung *et al.* 2003). The Wyoming craton is characterized as a fast anomaly down to approximately 400 km, suggesting a deep lithospheric root, which might explain the high surface elevation of this region.

Beneath 300 km, again similar to the starting model, shear wave-speed anomalies are significantly reduced to around 2 per cent. Two fast anomalies are observed beneath the Cascadia subduction zone, which are similar to observations made by Sigloch (2011). The northern one is mapped at great depth (around 700–800 km) while the southern one is imaged lying flat within the mantle transition zone. Below the mantle transition zone at 700 km depth, an elongated north-south fast anomaly is observed beneath the central and eastern US. This fast anomaly was observed previously in global-scale body-wave tomography and was interpreted as subducted lithosphere of the Farallon slab (Grand 1994; Grand *et al.* 1997; van der Hilst *et al.* 1997). At a depth of 800 km, our resolution starts to degrade (see Fig. 4), which may explain the lack of prominent fast anomalies at this depth beneath the central and eastern US. A very prominent slow anomaly is observed from 550 km to 800 km beneath the East Coast; the origin of this anomaly requires further investigation.

4.2 Vertical cross-sections of US_{22}

In Fig. 11 we present seven vertical cross-sections of US_{22} for the western US. Four horizontal cross-sections (at depths of 80, 400,

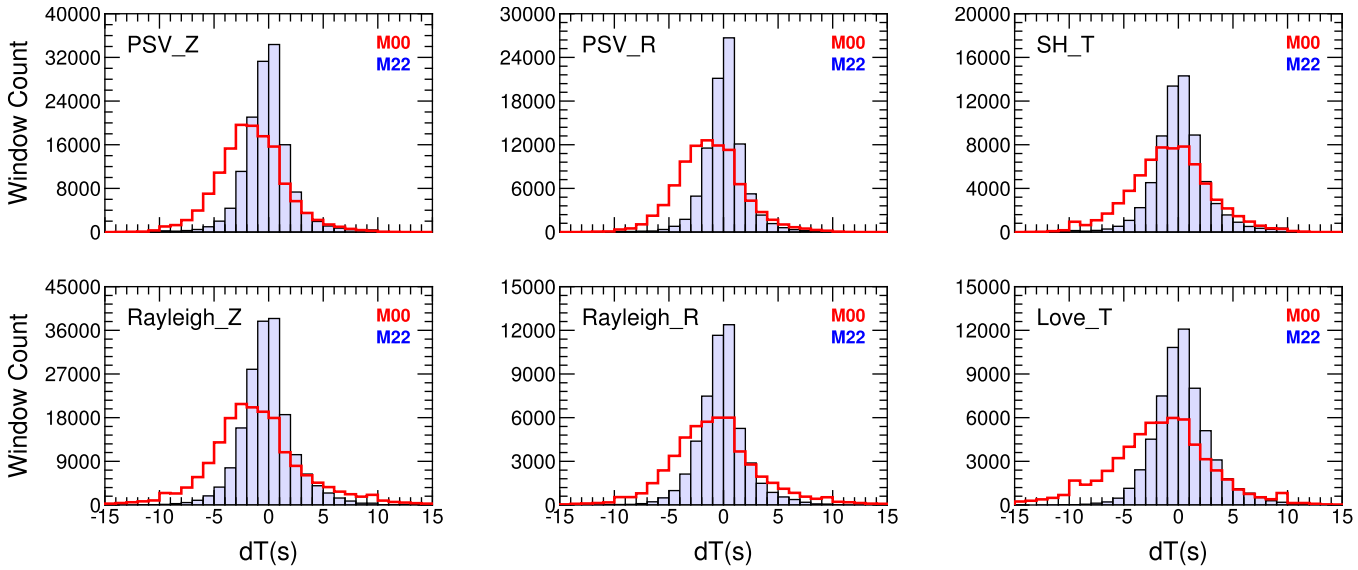

Figure 7. Comparison of histograms for phase measurements between starting model US_{00} (red) and final model US_{22} (blue). The top panels show three-component body-wave results, while the bottom panels show three-component surface-wave results.

600 and 800 km) are shown in the left panel of Fig. 11. Geologic provinces are shown by black lines. In cross-sections 1–3, at shallow depths, we observe a sharp contrast between the fast eastern US and the slow western US. The thickness of the lithosphere is 250–300 km. Beneath 660 km, we observe fast anomalies, which might be the northern part of the Cascadia slab. These fast anomalies are not directly connected to the surface, either due to a lack of resolution or reflecting a torn slab (Wortel & Spakman 2000). These fast wave-speed features are very prominent in the horizontal cross-section at 800 km depth. In cross-section 3, beneath Yellowstone, we observe slow anomalies at shallow depths and below the mantle transition zone. However, there are no continuous upwellings from the lower mantle to the Earth's surface. In cross-sections 4 and 5, we observe a fast anomaly lying flat within the mantle transition zone, which might be the southern part of the Cascadia slab. Based on vertical cross-sections 4 and 5 and a horizontal cross-section at 400 km depth, there might be interaction between the Cascadia slab and the deep root of the Wyoming craton.

In Fig. 12, we present six vertical cross-sections of US_{22} for the eastern US. Five horizontal cross-sections (at depths of 80, 400, 600, 700, and 800 km) are shown for reference. In these vertical cross-sections, we observe a pronounced fast wave-speed layer corresponding to the North American lithosphere with a thickness of about 300 km. The boundary between the lithosphere and underlying mantle is very sharp, and is not resolved in most body-wave tomographic models. In all cross-sections, slow wave-speed channels are imaged beneath the continental lithosphere, which are probably related to the weak asthenosphere. In cross-sections 1 and 2, we observe fast anomalies within the mantle transition zone. Their origin requires further investigation. In cross-sections 3–5, there are intriguing fast wave-speed downwellings beneath the thick continental lithosphere, which might reflect lithospheric delamination. These features have not been reported previously in body-wave studies due to possible vertical smearing as a consequence of the steep incidence of body waves. In cross-sections 5 and 6, there is a prominent fast anomaly below 660 km depth, which might be the subducted Farallon slab.

We present four long vertical cross-sections across the entire US in Supporting Information Fig. S5. Features discussed previously are further highlighted in these cross-sections. For instance, at shallow depths, we clearly see the wave-speed transitions from the western US to the North American lithosphere and then to the western Atlantic. At greater depths, we do not find direct connections between the Farallon slab beneath the mantle transition zone and other fast anomalies within the upper mantle. Several locations with possible lithospheric delamination are observed in cross-sections B-b and C-c. In cross-section B-b, the flat-lying Cascadian slab might interact with the fast wave-speed root beneath the Wyoming craton. In cross-section D-d, there are pronounced lower mantle slow anomalies beneath the West and East Coasts.

4.3 Comparisons with previous tomographic models

In this section we compare the isotropic shear wave-speed structure of US_{22} with several body- and surface-wave tomographic models developed over the past ten years. Models used for comparisons can be roughly divided into three groups. Models in the first group are constructed mainly based on surface-wave measurements, either dispersion curves or waveforms. These include Yuan14 (Yuan *et al.* 2014), Bedle09 (Bedle & van der Lee 2009) and Nettles08 (Nettles & Dziewoński 2008). Bedle09 is an isotropic shear wave-speed model constructed based on Rayleigh waves, while Nettles08 involves radial anisotropy and Yuan14 includes both radial and azimuthal anisotropy. In this study, we calculate their Voigt averages to obtain isotropic shear wave speeds. Models in the second group were constructed based on both *P*- and *S*-wave traveltimes, including Schmandt14 (Schmandt & Lin 2014) and Porritt14 (Porritt *et al.* 2014). Here we only discuss the isotropic shear wave-speed models. The third group includes two *P* wave-speed models built based on P-wave traveltimes, including Sigloch11 (Sigloch 2011) and Burdick14 (Burdick *et al.* 2013). We compare these models at four different depths: 80, 300, 500, and 700 km. Most surface waves only have good resolution at depths shallower than 300–400 km, therefore, at greater depths, we only compare US_{22} with body-wave models. A global-scale tomographic model, Simmons12 (Simmons *et al.* 2012), is also included in comparisons at depths of 500 km and 700 km. Since the available models each

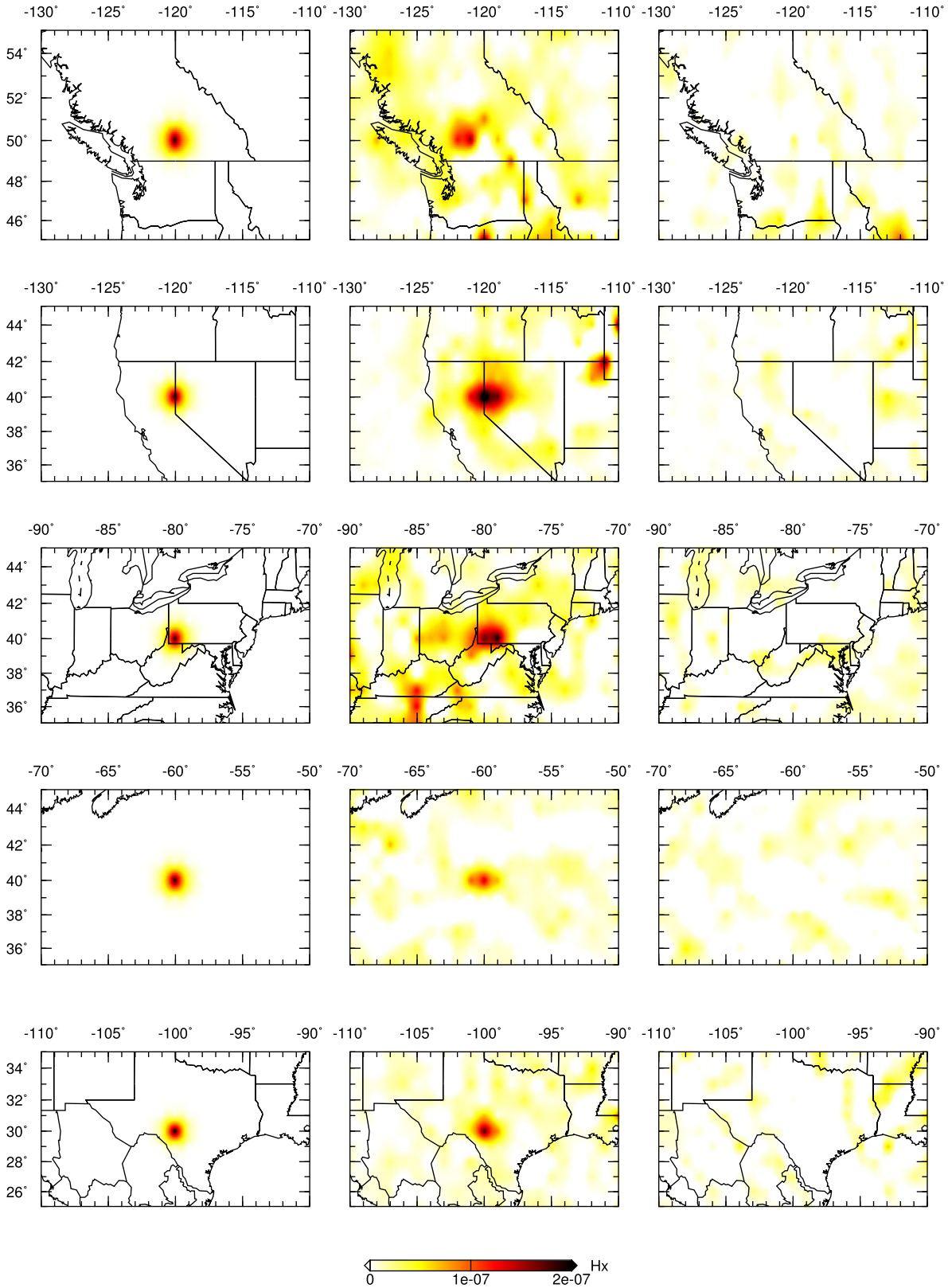

Figure 8. Point-spread function tests at a depth of 200 km. Left panel: locations of Gaussian vertically polarized shear wave speed (β_v) perturbations in US_{22}. Middle and right panel: point-spread functions with respect to vertically and horizontally polarized shear wave speeds, respectively. Note that there is little trade-off between β_v and β_h. From top to bottom are results for southern British Columbia, western Nevada, southwestern Pennsylvania, the western Atlantic, and southwestern Texas, respectively.

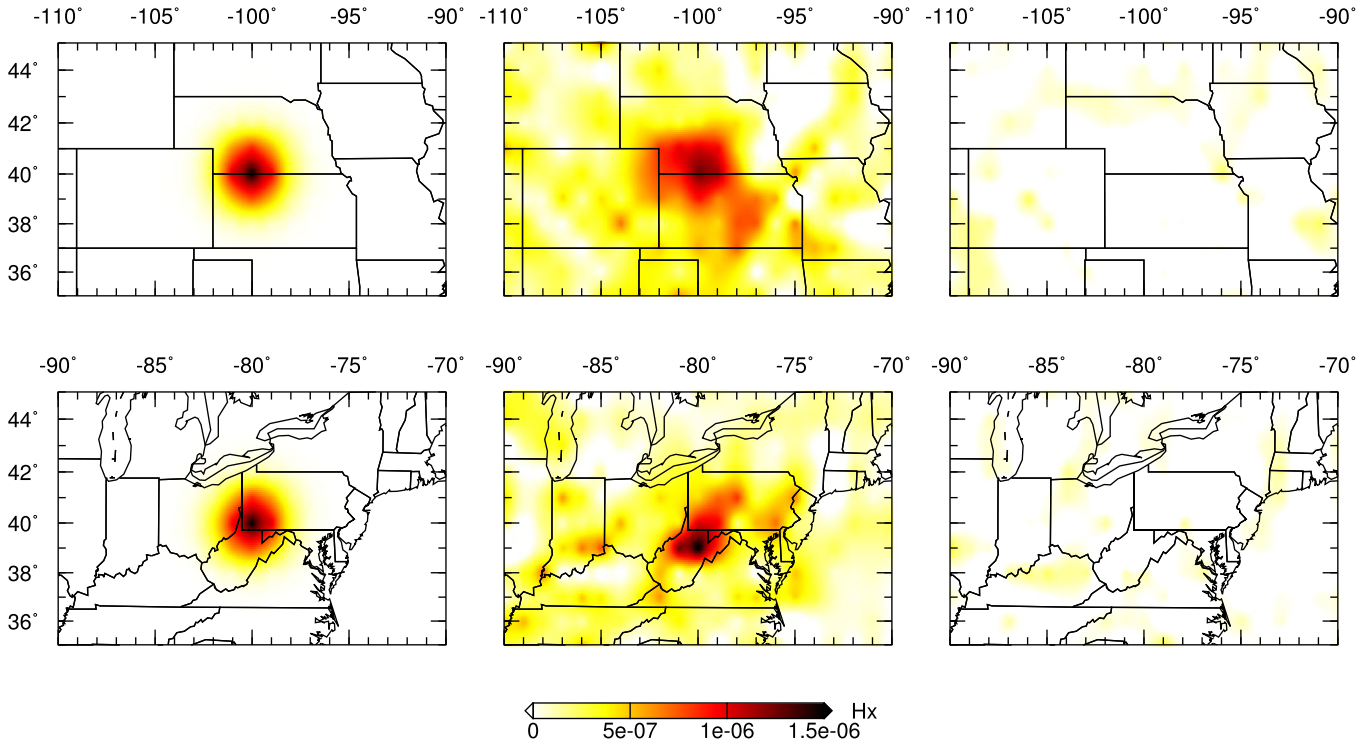

Figure 9. Map views of point-spread function tests at a depth of 500 km. Left panel: locations of Gaussian perturbations in US_{22} for the central and eastern US. Middle and right panel: point-spread functions with respect to vertically and horizontally polarized shear wave speeds, respectively.

have their own discretization, we present horizontal slices of these models at depths nearest to 80, 300, 500, and 700 km.

In Fig. 13 we compare these eight models at a depth around 80 km. The surface-wave models all feature a distinct wave-speed contrast between the slow western US and the fast eastern US, which correlates with the Rocky Mountain Front. This contrast is only significant in the body-wave models of Schmandt14 and Burdick14. In most surface-wave models, the cratonic region is dominated by contiguous fast wave speeds. In the body-wave models of Sigloch11 and Porritt14 the cratonic region involves numerous small-scale heterogeneities which are not present in US_{22} and the surface-wave models. On the other hand, complicated, small-scale features in the western US are present in body-wave models, such as the Snake River Plain. These are generally not very clear in surface-wave models, probably as a result of limitations in surface-wave frequency content. Overall, at this depth, the magnitude of shear wave-speed perturbations is consistent between US_{22} and the surface-wave models. Model Porritt14 is generally too weak.

At a depth of 300 km (Fig. 14) the cratonic region is dominated by fast wave speeds in most models, suggesting that we are still in the North American lithosphere. However, in terms of small-scale details, there are large discrepancies among different models. For instance, the western US is characterized by fast wave speeds in Bedle09 and Nettles08, while it is dominated by slow wave speeds in other models. The Snake River Plain is characterized as a prominent slow anomaly only in Porritt14 at this depth. Models US_{22}, Sigloch11, and Burdick14 are in reasonable agreement at this depth.

Within the mantle transition zone (Fig. 15), since the resolution of surface-wave tomography degrades at these depths, we only compare US_{22} with body-wave models. In addition, we included global model Simmons12 in the comparison. The similarities among different models are relative poor at this depth, suggesting that the mantle transition zone is a difficult region to constrain with body-wave tomography. Models US_{22} and Sigloch11 are in closer agreement than the other four models. For instance, both models feature fast wave-speed anomalies beneath the West and East Coasts. Although Schmandt14, Burdick14, and Porritt14 have pronounced fast anomalies beneath the eastern US, it is difficult to assess their uncertainty due to possible vertical smearing in body-wave inversions, which might project deep cratonic lithosphere down to the mantle transition zone.

At a depth of 700 km (Fig. 16), a fast anomaly which might reflect the ancient Farallon slab is recognized in all models. The geometry of this fast anomaly is similar in US_{22} and Porritt14. A slow anomaly is observed beneath Yellowstone in all six models. However, at this depth, there are a number of prominent slow anomalies which are much more significant than Yellowstone, such as features beneath the East Coast and the Gulf of California. Strong slow anomalies beneath the East Coast are prominent in US_{22}, Sigloch11, and Schmandt14. In addition, both US_{22} and Porritt14 include strong, localized slow anomalies beneath the Gulf of California.

Based on these comparisons, we conclude that at long wavelengths there is reasonably good agreement among different tomographic models. However, on smaller scales the level of agreement is relatively poor. Clearly we would like to see much more consensus between different models for robust geological interpretations, for instance to infer thermal structures and tectonic evolution.

5 RADIALLY ANISOTROPIC RESULTS

5.1 Comparisons with previous radially anisotropic studies

In this section we compare the radially anisotropic structure of US_{22} with two previous surface-wave studies, namely, Nettles08 (Nettles

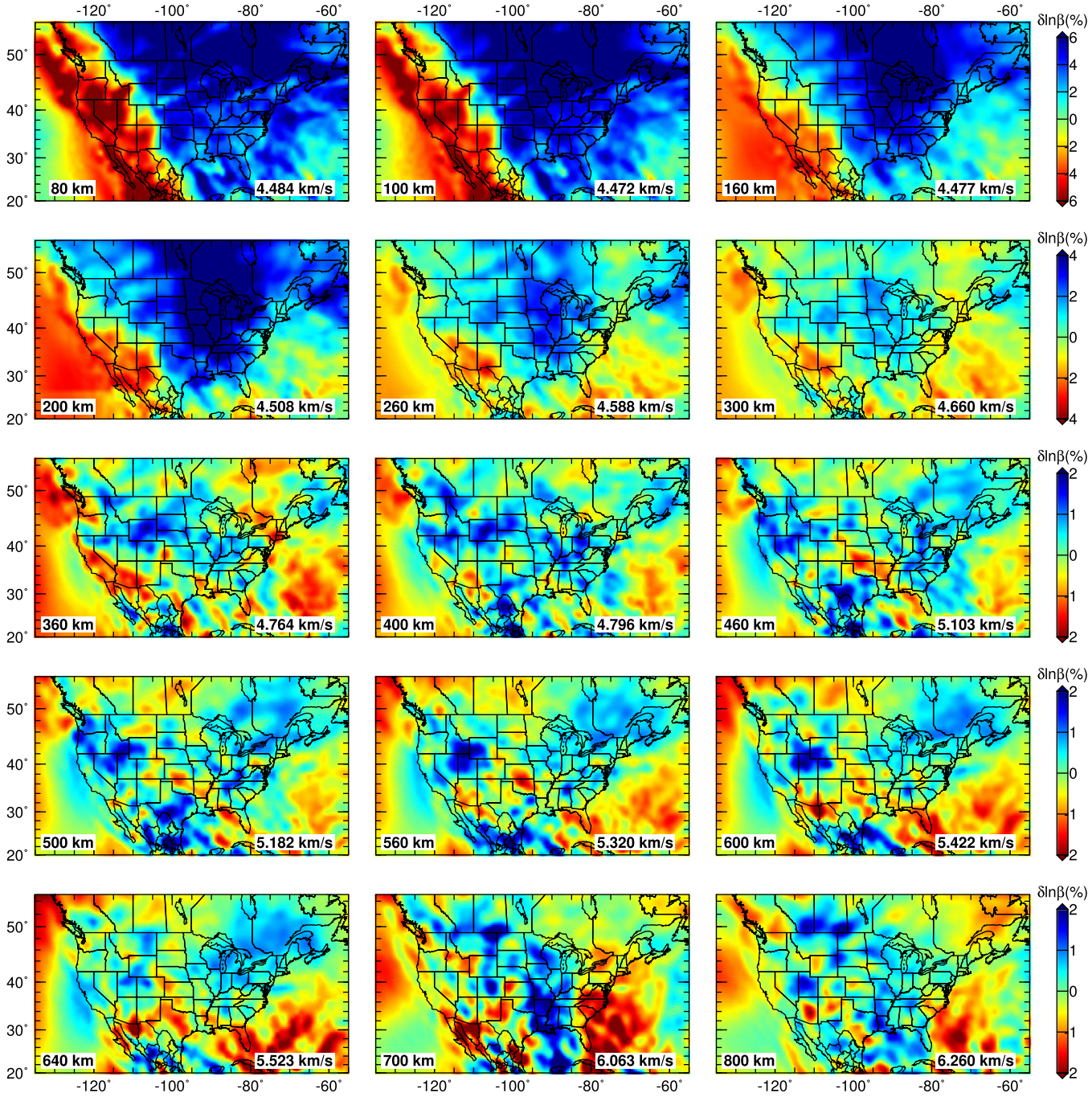

Figure 10. Horizontal cross-sections of relative perturbations in isotropic shear wave speed for US_{22} at depths ranging from 80 to 800 km. 1-D reference model STW105 (Kustowski *et al.* 2008) is used to compute the relative perturbations.

& Dziewoński 2008) and Yuan11 (Yuan *et al.* 2011). In order to suppress potential roughness in ξ introduced by the inversion for β_v and β_h, we applied Gaussian smoothing with a width of 150 km. Fig. 17 compares these three models at depths ranging from 70 to 300 km. Overall, they are similar at long-wavelengths, except that the magnitude of radial anisotropy in Yuan11 is relatively small in comparison with US_{22} and Nettles08. At a depth of 70 km, the entire continent is characterized by $\xi > 1$ in both US_{22} and Nettles08. Some short-wavelength features immediately underlying the continental crust might be due to crustal effects on β_v and β_h (Nettles & Dziewoński 2008). Therefore, the interpretation of radial anisotropy at this depth should be cautious. From 100 to 200 km, the eastern Pacific and western Atlantic are characterized by $\xi > 1$ in all three models, while beneath continental areas the similarities amongst these models are relatively poor. Below 200 km, radial anisotropy switches from $\xi > 1$ to $\xi < 1$. For instance, regions with $\xi < 1$ are observed beneath the western US in all three models, suggesting the robustness of this feature. The magnitude of this anomaly in US_{22} is relatively large in comparison with Nettles08 and Yuan11.

Several vertical cross-sections are presented in Figs 18 and 19. The different pattern of radial anisotropy beneath the continent and the oceans stands out. For instance, in both US_{22} and Nettles08, the eastern Pacific and western Atlantic involve channels with $\xi > 1$ from 100 to 200 km. Beneath the continent, a similar pattern is

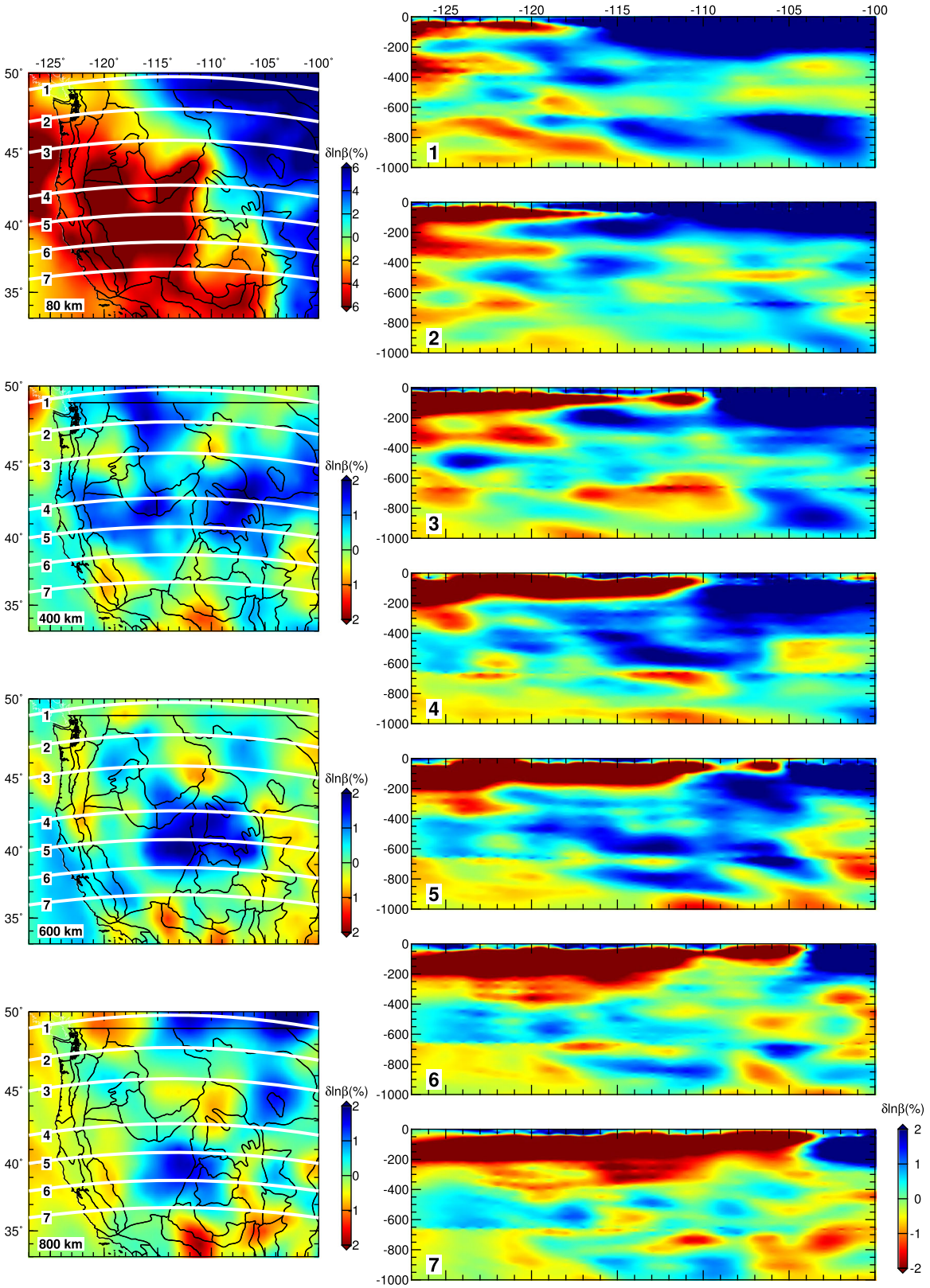

Figure 11. Map views and vertical cross-sections of relative perturbations in isotropic shear wave speed in US_{22} for the western US. The left panel shows map views and locations of seven vertical cross -sections. The right panel shows these sections. Zoom in version from 0 to 400 km can be found in Supporting Information Fig. S3.

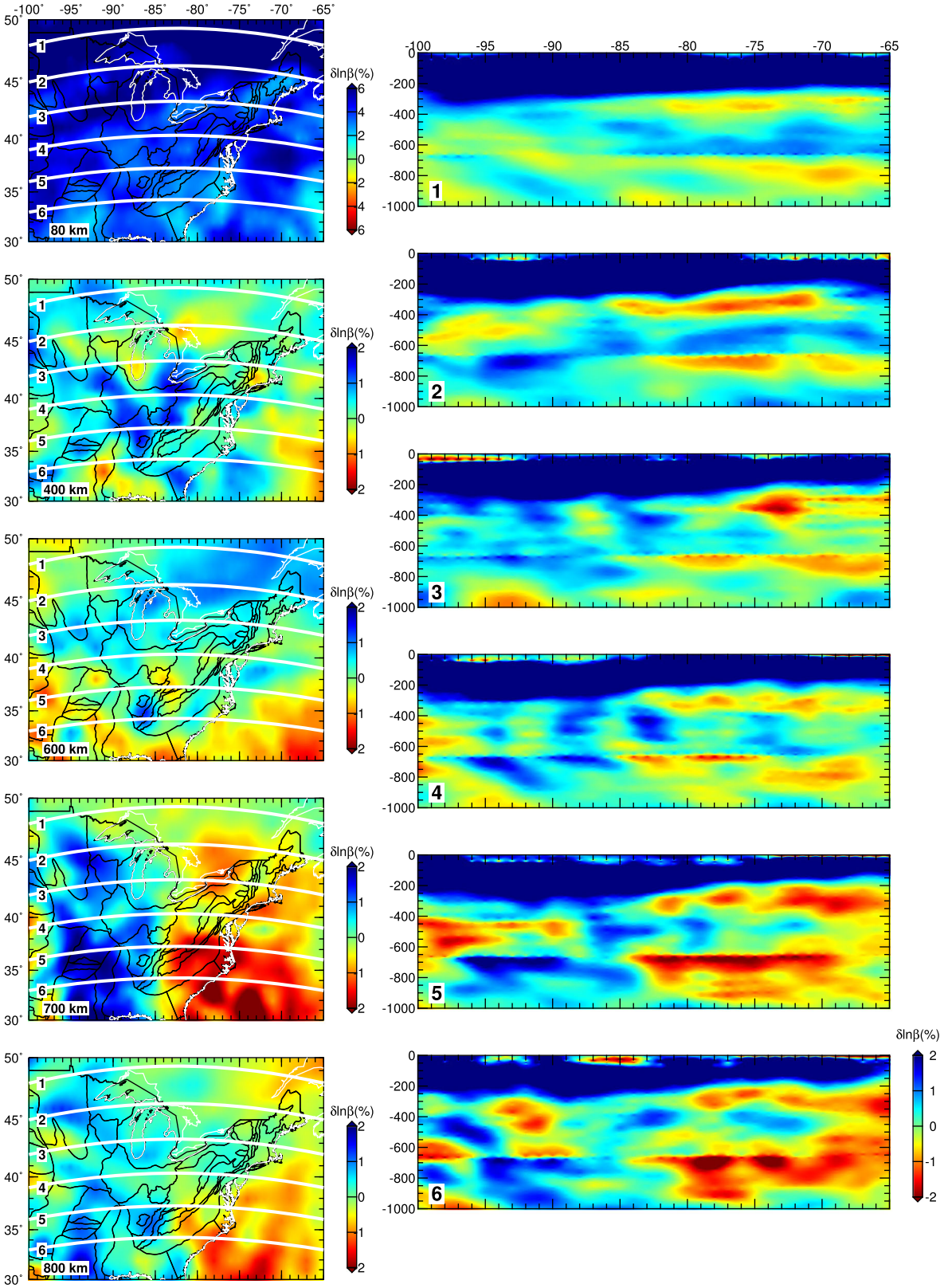

Figure 12. Same as Fig. 11 but for the eastern US. Zoom in version from 0 to 400 km can be found in Supporting Information Fig. S4.

observed at shallower depths (<150 km). Such differences between oceans and continents are not as clear in Yuan11 in comparison with US_{22} and Nettles08. Regions with $\xi < 1$ can be easily identified beneath the western US in Figs 18 and 19. Based on Figs 17–19, we conclude that these three models are similar at long wavelengths, however, there are still large disagreements in terms of small-scale details. Several issues which might contribute to these disagreements are discussed in Section 6.

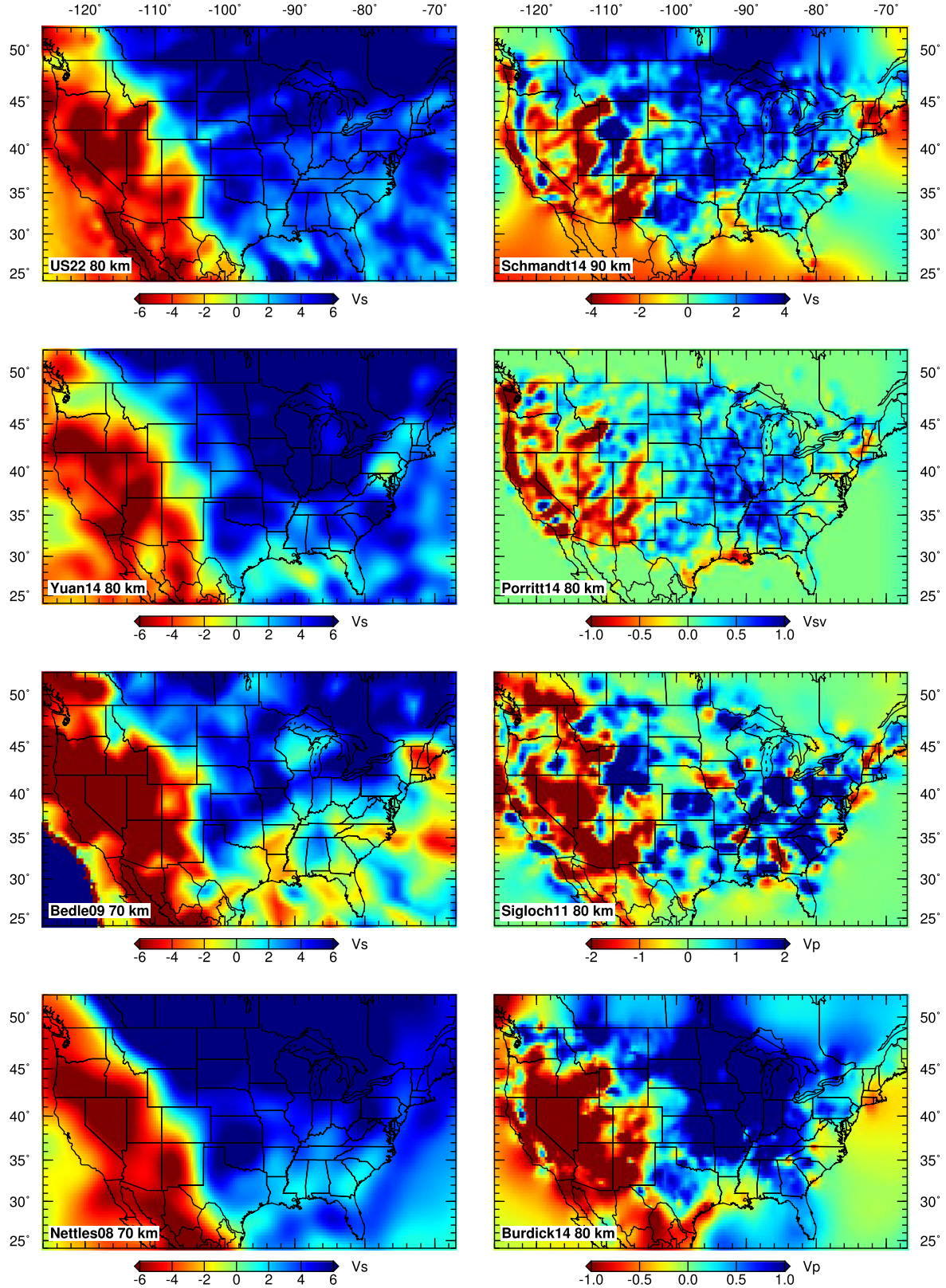

Figure 13. Comparison of the isotropic shear wave-speed structure of US_{22} with several previous tomographic models at 80 km. Shown are three surface-wave models, namely, Yuan14 (Yuan *et al.* 2014), Bedle09 (Bedle & van der Lee 2009) and Nettles08 (Nettles & Dziewoński 2008), and four body-wave models, namely, Schmandt14 (Schmandt & Lin 2014), Porritt14 (Porritt *et al.* 2014), Sigloch11 (Sigloch 2011) and Burdick14 (Burdick *et al.* 2013). Most models are collected from the IRIS Earth Model Center (EMC) (http://ds.iris.edu/ds/products/emc/).

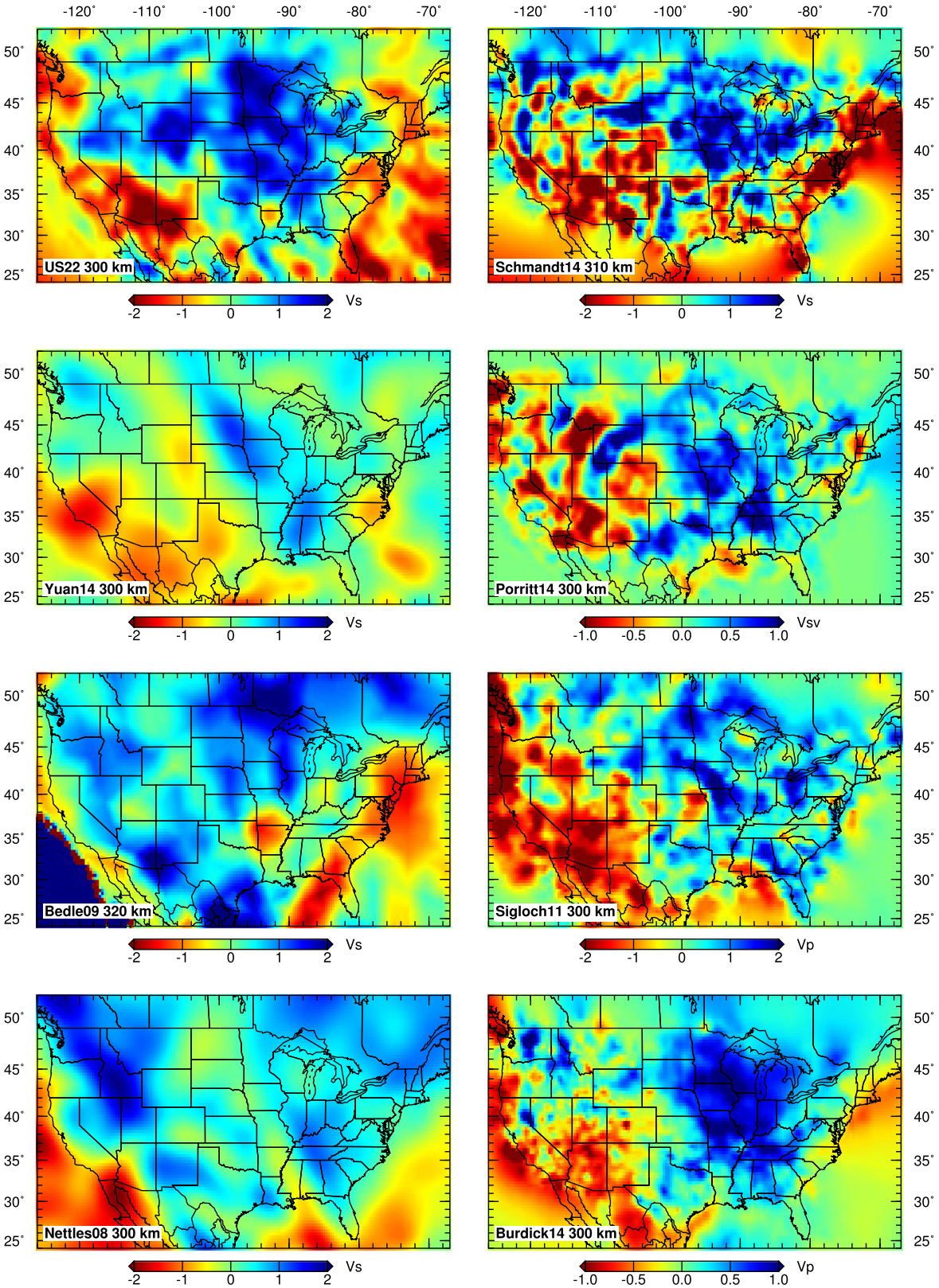

Figure 14. Same as Fig. 13 but at a depth of 300 km.

5.2 Average 1-D radial profiles

In this section, we divide the study area into six tectonically distinct provinces: the eastern Pacific, the western US, the Superior Craton, the southern US, the eastern US and the western Atlantic. Their geometry is shown in different colours in the top panel of Fig. 20. We plot average 1-D radial profiles of isotropic shear wave speed β and the radially anisotropic parameter ξ for these six provinces in Fig. 20. 1-D reference model STW105 (Kustowski *et al.* 2008) is used for comparison. For the isotropic shear wave speed, large

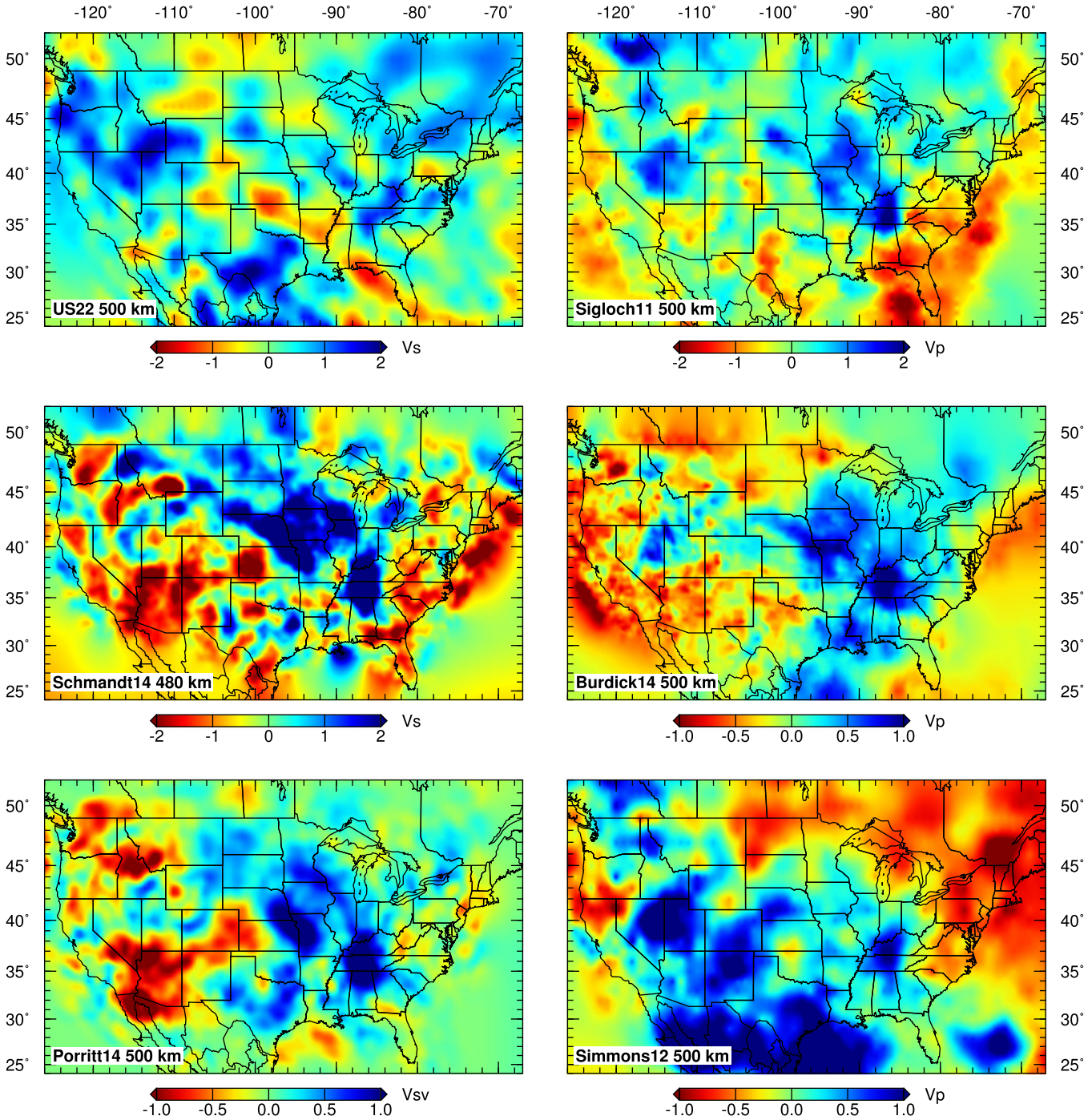

Figure 15. Comparison of the isotropic shear wave-speed structure of US_{22} with body-wave models at a depth of 500 km. Global body-wave model Simmons12 (Simmons *et al.* 2012) is also included for comparison.

anomalies correlated with surface tectonics exist at depths shallower than 300 km. For instance, prominent shear wave-speed reductions are observed beneath the eastern Pacific and the western US, while the Superior craton, southern and eastern US, and western Atlantic are characterized by fast wave speeds. At depths greater than 300 km, the magnitude of the anomalies reduces rapidly.

For the eastern Pacific and western Atlantic, values of $\xi > 1$ are observed from 50 to 300 km with maximum values around depths of 150 km. Values of $\xi < 1$ at depths shallower than 50 km come from the starting model S362ANI (see Supporting Information Fig. S1), and have been analysed previously by Ekström & Dziewoński (1998). The eastern Pacific and western Atlantic have different shear wave speed characteristics at these depths, reflecting differences between active and passive continental margins.

Beneath the western US, we observe significant reductions in isotropic shear wave speed at depths shallower than 200 km. For ξ, there is a peak with a magnitude greater than 1.1 at a depth around 100 km. Its magnitude reduces gradually to 1.0 around 250 km. Below this depth, the pattern switches to $\xi < 1$, correlating with patterns at depths from 300 to 400 km in Fig. 17. Similar depth profiles have been observed by Nishimura & Forsyth (1989) for young Pacific Plate (<4 Ma yr old) based on surface-wave inversion.

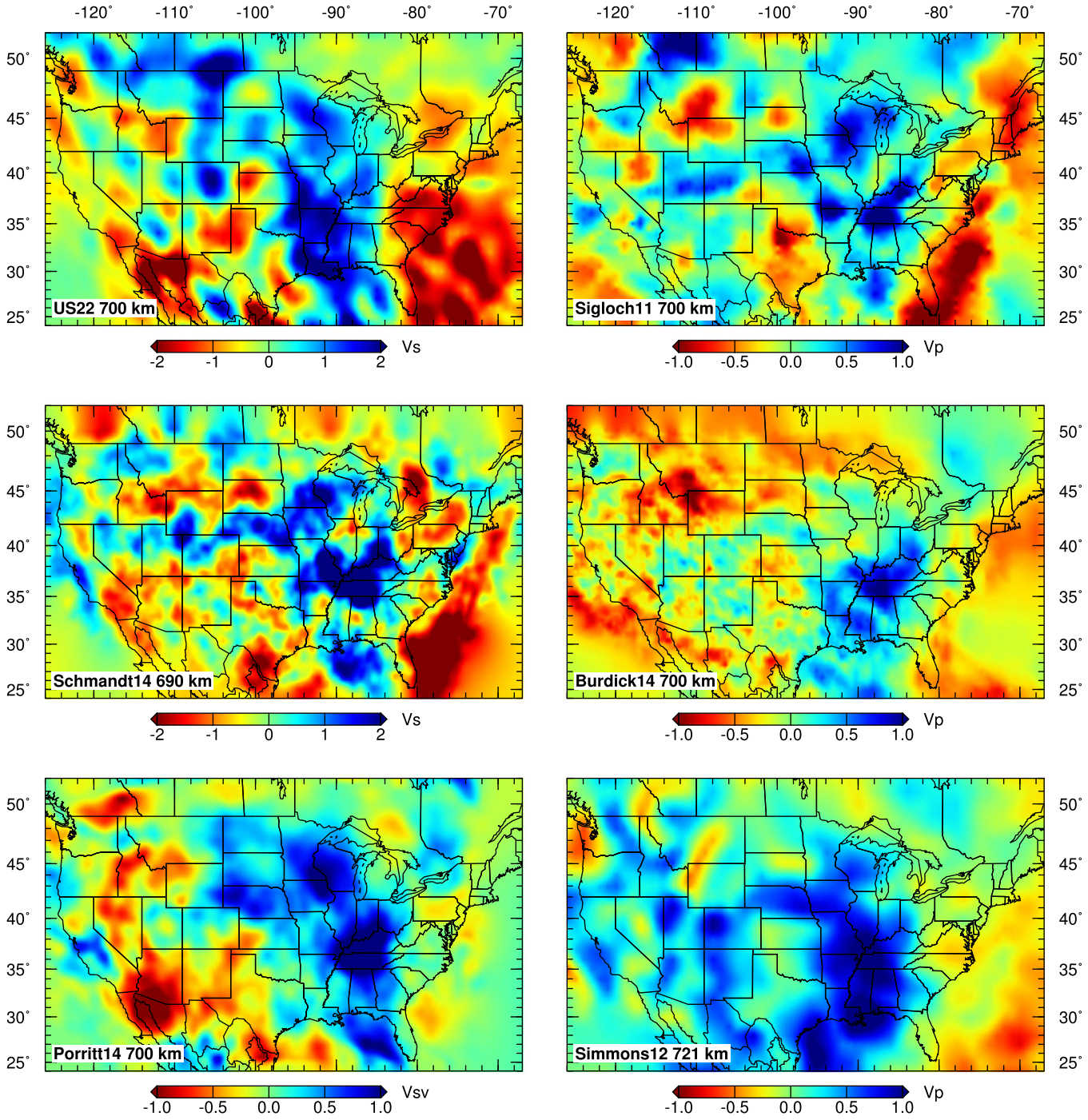

Figure 16. Same as Fig. 15 but at a depth of 700 km.

They interpreted $\xi < 1$ at great depths in terms of upwellings beneath oceanic ridges.

For continental areas (the Superior Craton and the southern and eastern US), the behaviour of radial anisotropy is similar to the western US at depths shallower than 300 km, but with smaller magnitudes. Only the southern US is observed to have relatively weak $\xi < 1$ below 300 km. In US_{22}, underneath continental areas, no shear zones with $\xi > 1$ are observed at depths greater than 300 km, as suggested previously by Gung *et al.* (2003). Fast wave speeds at depths shallower than 250–300 km are observed for all continental areas, representing the continental lithosphere. In addition, the Superior Craton has a deep root around 300–350 km.

5.3 Correlations between $\delta \ln\beta$ and ξ

In order to analyse statistical correlations between isotropic shear wave speed and radial anisotropy, following Huang *et al.* (2010), we plot 2-D correlation diagrams between these two parameters at different depths for the six tectonic provinces. Correlations between these two parameters may provide insights with regards to the origins of anisotropy. Huang *et al.* (2010) observed clear anti-correlations between shear wave speed and radial anisotropy within the middle to lower crust beneath Tibet, for instance, $\delta \ln\beta < 0$ and $\xi > 1$. We observe a similar pattern for the eastern Pacific and western US at depths shallower than 200 km (Fig. 21). The

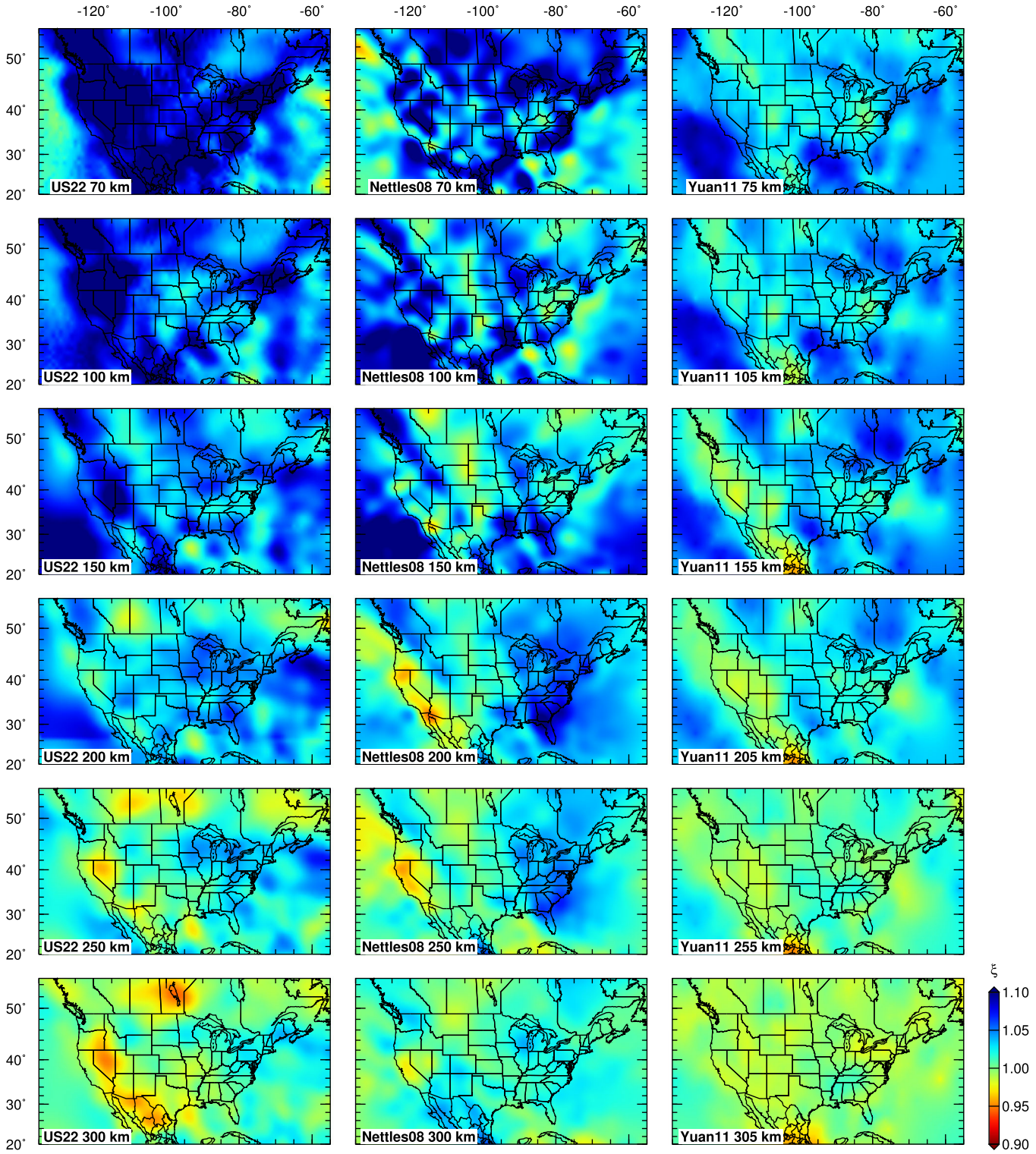

Figure 17. Comparison of the radially anisotropic structure of various models at depths ranging from 70 to 300 km. From left to right are shown US_{22}, Nettles08 (Nettles & Dziewoński 2008) and Yuan11 (Yuan *et al.* 2011).

pattern for the eastern Pacific at 50 km ($\xi < 1$) comes from starting model US_{00}. Overall, in this depth range, the eastern Pacific and the western US are characterized by slow wave speeds $\delta \ln \beta < 0$ and horizontal shear $\xi > 1$, which might suggest strong LPO and weak materials/high temperatures within the asthenosphere. The pattern for the western Atlantic is different from the Pacific and western US. It is dominated by $\delta \ln \beta > 0$ and $\xi > 1$, which might suggest a different origin of anisotropy. The passive margin of the western Atlantic is similar to continents in comparison with oceans (see Fig. 22). Below 250 km, the magnitudes of wave-speed perturbations and radial anisotropy reduce significantly. Most parts of the western US are dominated by $\xi < 1$, both fast and slow anomalies are observed with this type of radial anisotropy.

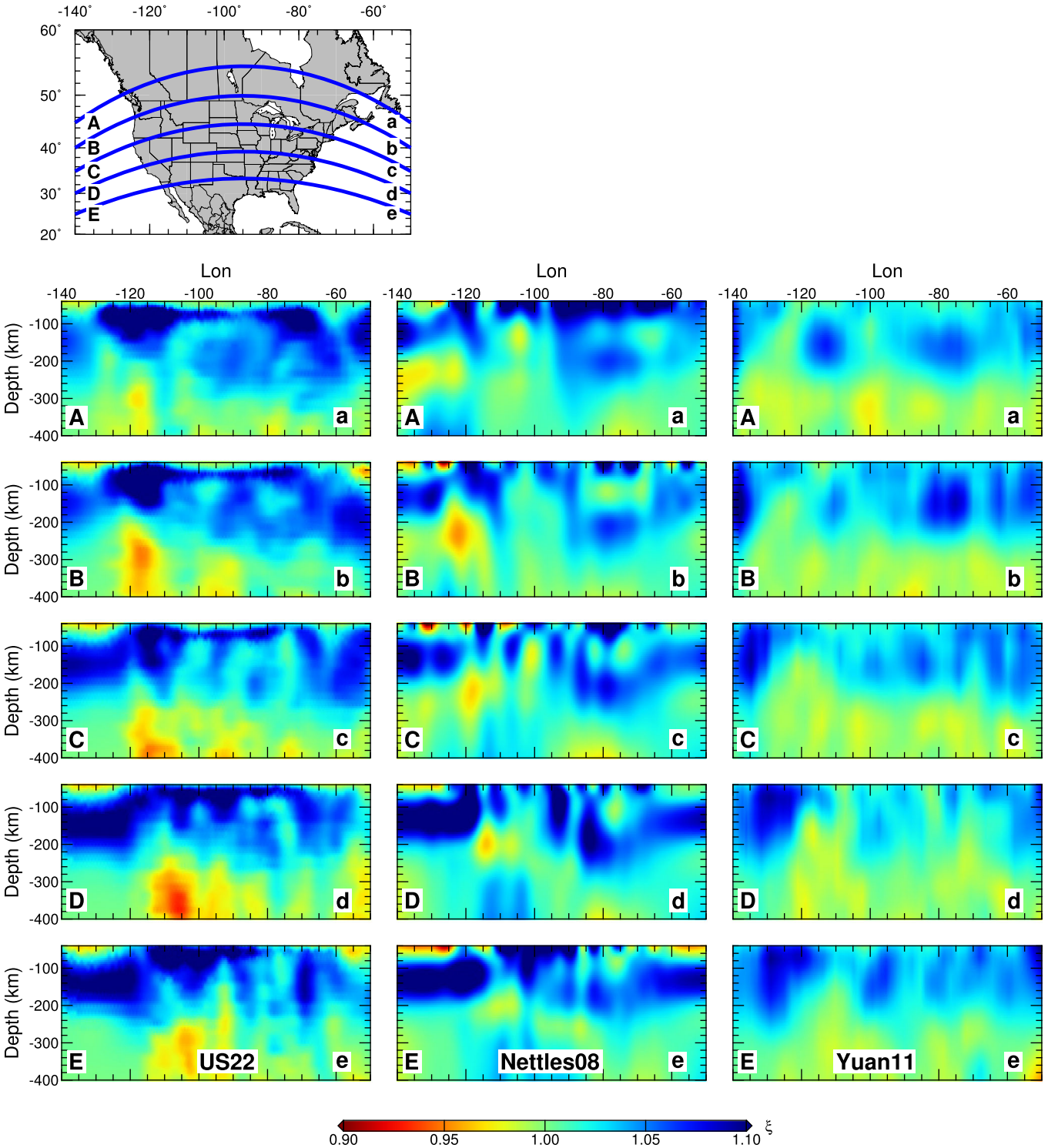

Figure 18. Comparison of vertical cross-sections of radially anisotropic heterogeneity at different latitudes for various models. The top panel shows the locations of the vertical cross-sections. From left to right are shown US_{22}, Nettles08 and Yuan11.

Continental areas (the Superior Craton, the southern and eastern US) are similar to the western Atlantic at depths shallower than 250 km, that is, with $\delta \ln \beta > 0$ and $\xi > 1$. From 250 to 300 km beneath the Superior Craton, there are values of $\xi < 1$, which might be related to downwellings beneath some parts of the craton. From 350 to 400 km, most continental regions involve relatively small perturbations in shear wave speed and radial anisotropy, except that regions with $\xi < 1$ are observed for the southern US at 400 km, which might reflect lithospheric delamination as suggested by the wave-speed models (see Supporting Information Fig. S5).

Slow shear wave-speed anomalies might indicate high temperatures and weak materials, which can easily develop LPO under shear strain. This may explain channel signatures beneath the eastern Pacific and western US at shallower depths. However, most continental regions and the western Atlantic are dominated by fast anomalies, which might indicate cold temperatures. Mineral physics

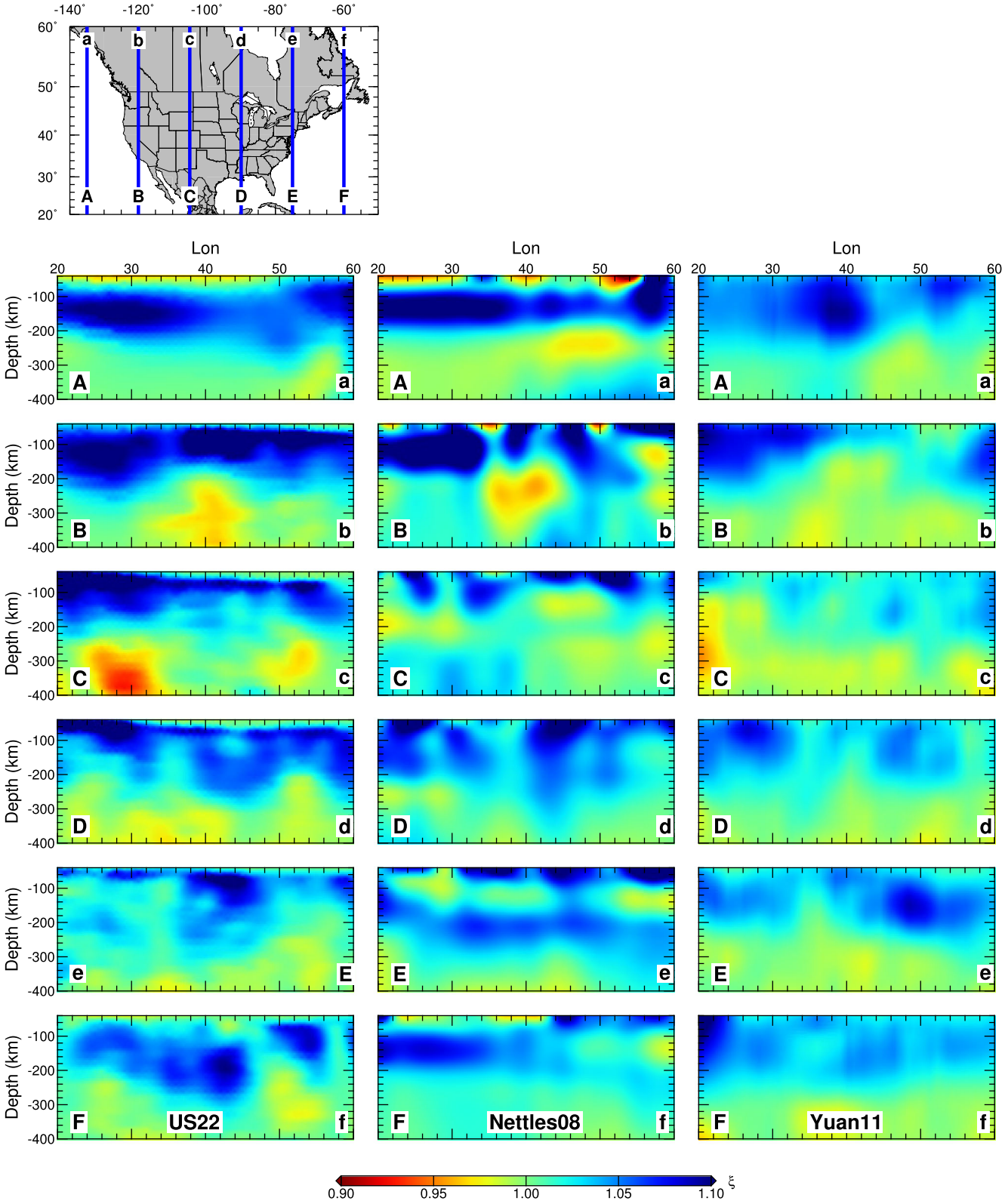

Figure 19. Same as Fig. 18 but for different vertical cross-sections.

experiments have shown that the mobility of olivine highly depends on temperature variations (Nicolas & Christensen 1987). The existence of $\xi > 1$ beneath continents may have different origins compared to oceans. 'Frozen-in' anisotropy (Silver 1996) is one possible interpretation.

6 DISCUSSION

As illustrated in Section 4.3, different tomographic studies are in good agreement for long-wavelength isotropic shear wave-speed variations, but there is strong disagreement on smaller scales, especially within the mantle transition zone. Several factors might

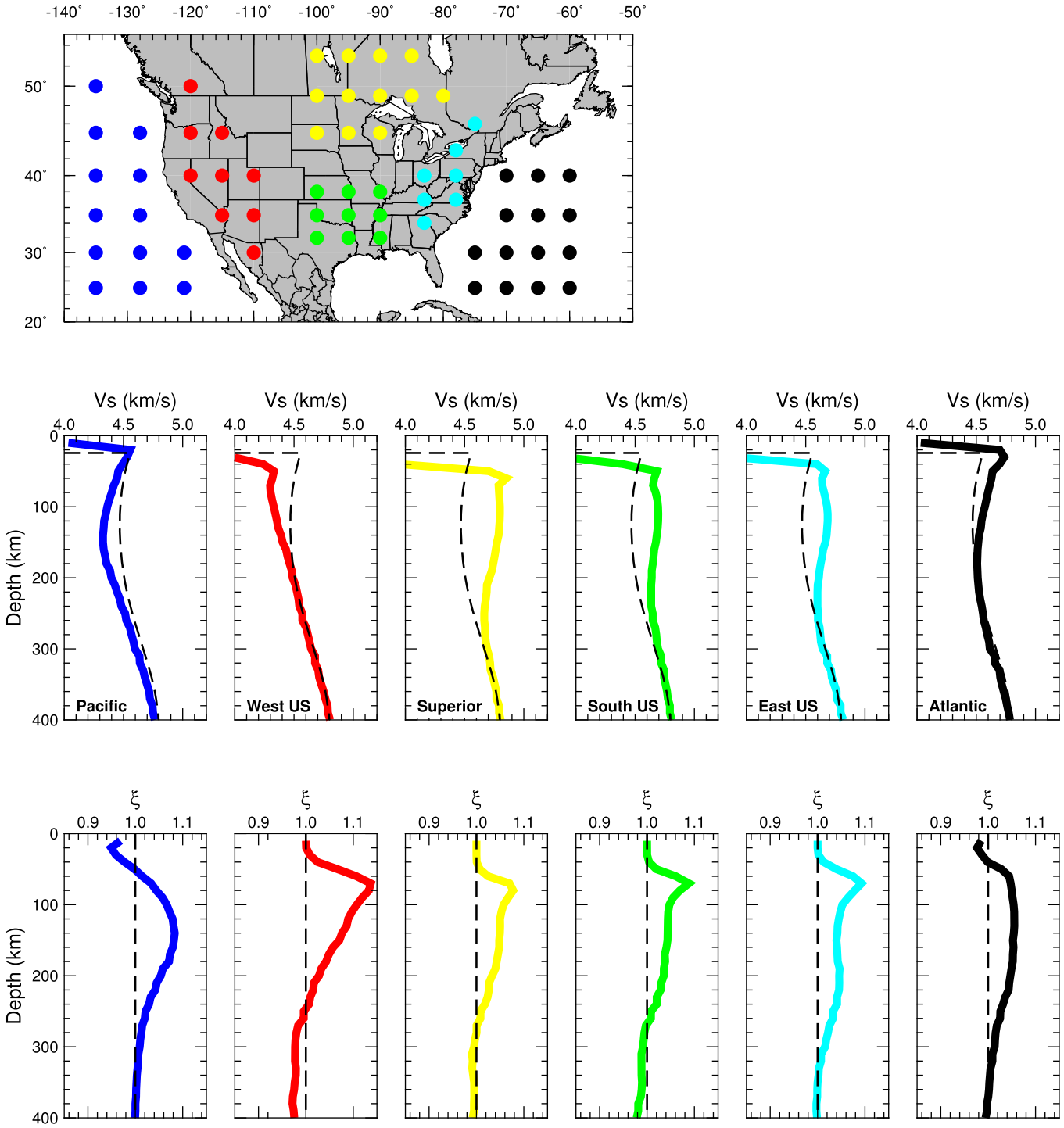

Figure 20. Average 1-D radial profiles for isotropic shear wave speed and the radially anisotropic parameter ξ for different tectonic provinces. The top panel shows the locations of the samples used to divide the studied region. The middle panel illustrates average 1-D depths profiles for isotropic shear wave speed. From left to right are results for the eastern Pacific, the western US, the Superior Craton, the southern US, the eastern US and the western Atlantic. The dashed lines are 1-D wave-speed profiles from STW105 (Kustowski *et al.* 2008). The bottom panel shows radial profiles of the radially anisotropic parameter ξ at different locations. The dashed lines are depth profiles for isotropic models with $\xi = 1$.

contribute to this, namely, non-uniqueness of geophysical inverse problems (Jackson 1972; Tarantola 2005), use of regularization, different measurements and their relative weights (Ritsema *et al.* 1999; Moulik & Ekström 2014, 2016), different 1-D reference models, different strategies for crustal corrections (Lekic *et al.* 2010; Panning *et al.* 2010), choices of model parameters, etc. All these issues contribute to the discrepancies observed in Section 4.3, making direct comparisons among different tomographic models a challenging task.

Agreements between radially anisotropic models is poor on both global and regional scales (Kustowski *et al.* 2008; Zhu *et al.* 2015). Several factors can influence the outcome of inversions for radial anisotropy, including data quality of Love- and Rayleigh-wave measurements, proper balancing of Love- and Rayleigh-wave

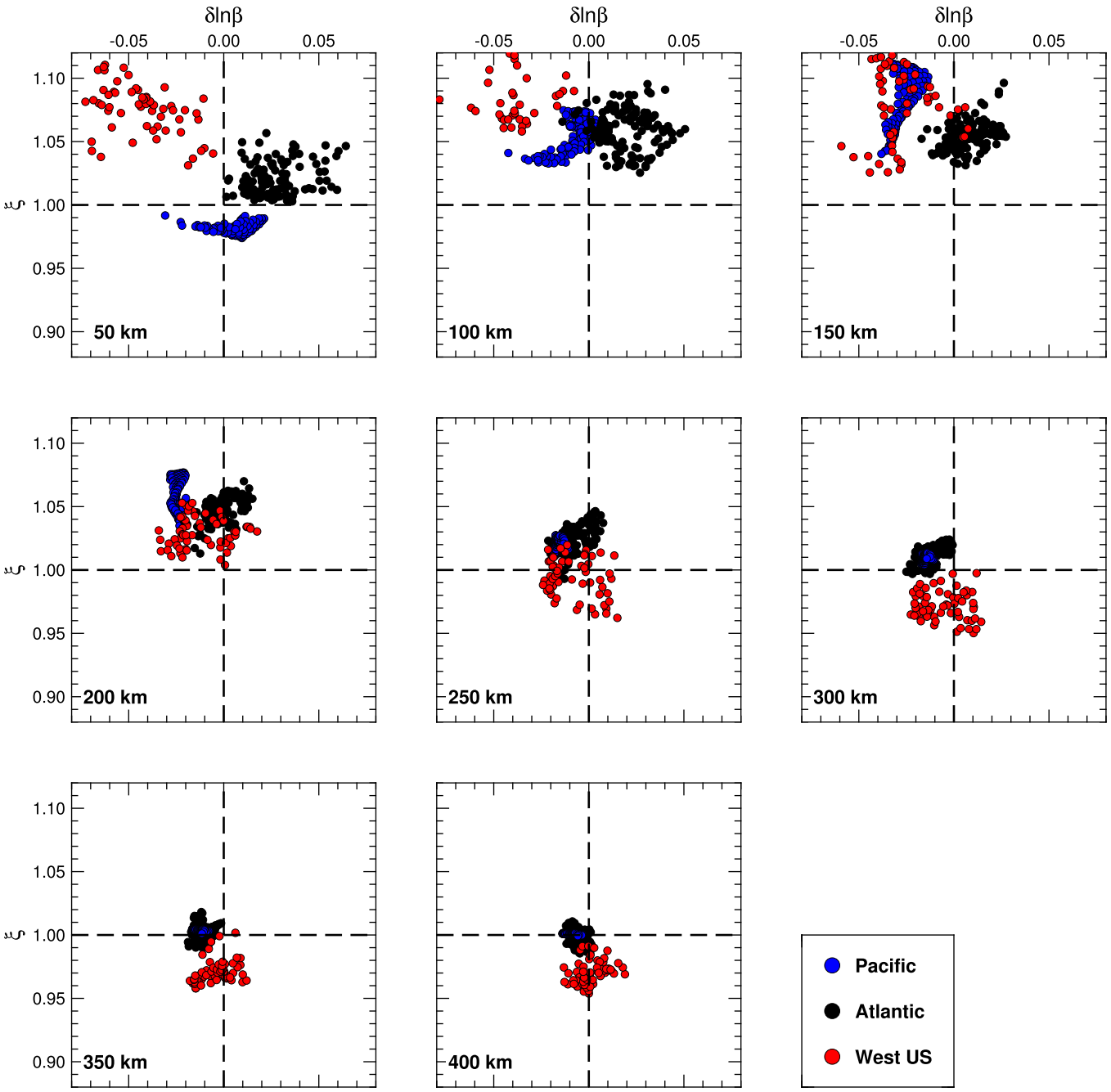

Figure 21. Correlation relation between isotropic shear wave-speed perturbations $\delta \ln \beta$ and the radially anisotropic parameter ξ at depths ranging from 50 to 400 km. Blue, black, and red dots are samples for the eastern Pacific, the western Atlantic, and the western US, respectively. The locations of these samples are labelled in Fig. 20.

contributions (Nettles & Dziewoński 2008), trade-offs between crustal and upper mantle anisotropy (Fichtner *et al.* 2010; Moschetti *et al.* 2010), trade-offs between vertically and horizontally polarized shear wave speeds, corrections for azimuthal anisotropy (Ekström 2011; Moulik & Ekström 2016), and more general anisotropy (Levin & Park 1997; Debayle *et al.* 2005).

In this study, we use the radially anisotropic parameter ξ as a proxy for plastic flow directions within the upper mantle, such that $\xi > 1$ reflects horizontal mantle flow while $\xi < 1$ reflects vertical mantle flow. Other possibilities might change our interpretations. Mineral physics experiments have established relations between seismic anisotropy and LPO for both single crystals and rock samples. However, it is challenging to relate LPO and mantle flow directions. For instance, in water enriched environments, A-type LPO changes to B- or C-type (Jung & Karato 2001). In such cases, $\xi > 1$ might correspond to vertical flow instead of horizontal flow. This transition has been used to explain complicated SKS signals observed above the mantle wedge (Long & Silver 2008). In addition, under simple shear conditions, LPO fabrics also depend on the magnitude of strain. Under relatively small shear strain, LPO aligns with finite-strain directions, while in a large strain regime it aligns with flow directions (Zhang & Karato 1995). All these factors add complexities to the interpretation of anisotropic models.

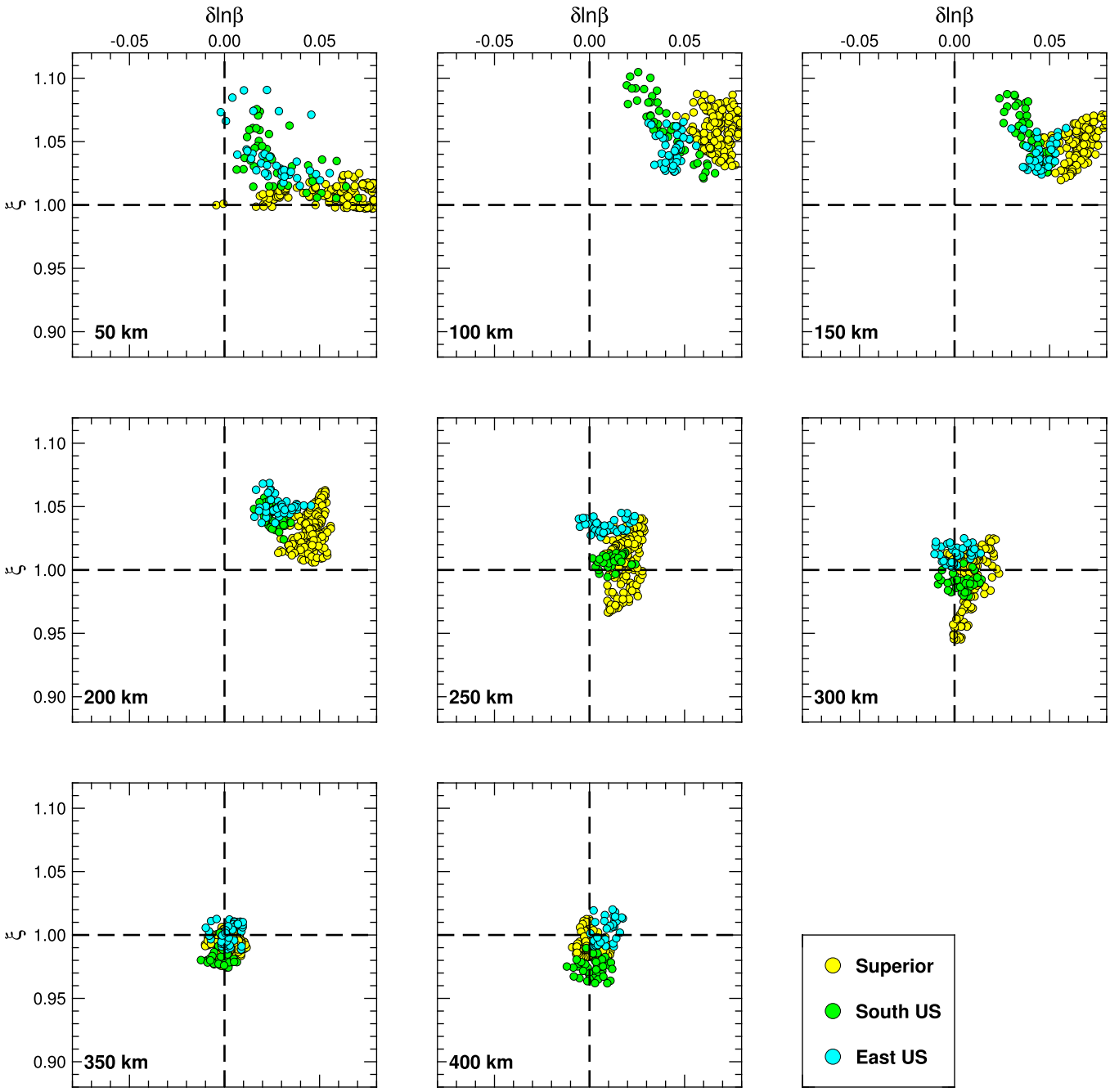

Figure 22. Same as Fig. 21 but for continental areas of the US. Yellow, green, and cyan dots are samples for the Superior Craton, the southern US, and the eastern US, respectively.

7 CONCLUSIONS

We have constructed a radially anisotropic model of the North American continent named US_{22}. This model is built based on adjoint tomography using three-component USArray data from 180 regional earthquakes. Short-period body waves (periods between 15 and 50 s) and long-period surface waves (periods between 25 and 150 s) are combined to simultaneously constrain deep and shallow structures. We observe a sharp lithospheric shear wave-speed contrast between the eastern and western US coincident with the Rocky Mountain Front. A nearly 400 km deep lithospheric root is observed beneath the Wyoming craton. Several fast shear wave-speed downwellings are observed beneath the thick North American lithosphere, which might reflect delamination. The ancient Farallon slab is mapped beneath the mantle transition zone of the central US. We do not observe a continuous lower to upper mantle upwelling beneath Yellowstone. Large-scale slow anomalies are mapped beneath the western US at shallow depths (<250 km) as well as beneath the West and East Coasts at greater depths (within the mantle transition). Slow wave-speed channels are imaged beneath the North American lithosphere in the eastern US, which might reflect the weak asthenosphere.

Radial anisotropy in US_{22} confirms different values of the radially anisotropic parameter $\xi = (\beta_h/\beta_v)^2$ beneath oceans and continents. Regions with $\xi > 1$ are imaged at depths from 100 to 200 km beneath oceans. However, underneath continents similar behaviour is imaged at shallower depths. Different wave-speed signatures are

observed associated with these anisotropic features, suggesting different origins of anisotropy beneath oceans and continents. For the western Atlantic passive margin, model characteristics at depths shallower than 200 km are more similar to continental areas than to the eastern Pacific. The western US is characterized by $\xi < 1$ from 300 to 400 km depths, which might be related to vertical flows induced by subduction of the Farrallon and Juan de Fuca Plates. A similar pattern is observed beneath the southeastern US, which might reflect lithospheric delamination.

ACKNOWLEDGEMENTS

Numerical simulations for this study were performed on the 'Lonestar4' and 'Lonestar5' computers located at the Texas Advanced Computing Center (TACC). We thank Dr Omar Ghattas for providing computational resources for this study. We acknowledge Dr Gabi Laske, Dr Barbara Romanowicz and one anonymous reviewer for their comments and suggestions that helped to improve the manuscript. Data analysis was performed on a Dell cluster at the Princeton Institute for Computational Science & Engineering (PICSciE). Waveform data used in this study are collected from the Incorporated Research Institutions for Seismology Data Management Center (IRIS DMC). Tomographic models used for comparisons were collected from the IRIS Earth Model Center (IRIS EMC). The open source spectral-element package SPECFEM3D_GLOBE and the seismic measurement software package FLEXWIN used in this study are freely available via the Computational Infrastructure for Geodynamics (CIG).

REFERENCES

Abercrombie, R. & Ekström, G., 2001. Earthquake slip on oceanic transform faults, *Nature,* **410,** 74–77.

Anderson, D., 1961. Elastic wave propagation in layered anisotropic media, *J. geophys. Res.,* **66,** 2953–2963.

Backus, G., 1962. Long-wave elastic anisotropy produced by horizontal layering, *J. geophys. Res.,* **67,** 4427–4440.

Backus, G., 1965. Possible forms of seismic anisotropy of the uppermost mantle under oceans, *J. geophys. Res.,* **70,** 3429–3439.

Bassin, C., Laske, G. & Masters, G., 2000. The current limits of resolution for surface wave tomography in North America, *EOS, Trans. Am. geophys. Un.,* **81,** F897.

Bedle, H. & van der Lee, S., 2009. S velocity variation beneath North America, *J. geophys. Res.,* **114,** doi:10.1029/2008JB005949.

Bensen, G., Ritzwoller, M., Barmin, M., Levshin, A., Lin, F., Moschetti, M., Shapiro, N. & Yang, Y., 2007. Processing seismic ambient noise data to obtain reliable broad-band surface wave dispersion measurements, *Geophys. J. Int.,* **169,** 1239–1260.

Bird, P., 1988. Formation of the Rocky Mountains, Western United States: a continuum computer model, *Science,* **239,** 1501–1507.

Bodin, T., Sambridge, M., Tkalcic, H., Arroucau, P., Gallagher, K. & Rawlinson, N., 2012. Transdimensional inversion of receiver functions and surface wave dispersion, *J. geophys. Res.,* **117,** B02301. doi:10.1029/2011JB008560.

Bozdağ, E.D., Peter, D., Lefebvre, M., Komatitsch, D., Tromp, J., Hill, J., Podhorszki, N. & Pugmire, D., 2016. Global adjoint tomography: first-generation model, *Geophys. J. Int.,* **207,** 1739–1766.

Bui-Thanh, T., Ghattas, O., Martin, J. & Stadler, G., 2013. A computational framework for infinite-dimensional Bayesian inverse problems, Part I: The linearized case, with application to global seismic inversion, *SIAM J. Sci. Comput.,* **35,** A2494–A2523.

Bunge, P. & Grand, S., 2000. Mesozoic plate-motion history below the northeast Pacific ocean from seismic images of the subducted Farallon slab, *Nature,* **405,** 337–340.

Bunks, C., Saleck, F.M., Zaleski, S. & Chavent, G., 1995. Multiscale seismic waveform inversion, *Geophysics,* **60,** 1457–1473.

Burdick, S. *et al.*, 2013. Model update January 2013: Upper mantle heterogeneity beneath North America from travel-time tomography with global and USArray transportable array data, *Seismol. Res. Lett.,* **85,** 77–81.

Calò, M., Bodin, T. & Romanowicz, B., 2016. Layered structure in the upper mantle across North America from joint inversion of long and short period seismic data, *Earth planet. Sci. Lett.,* **449,** 164–175.

Chen, M., Niu, F., Liu, Q., Tromp, J. & Zheng, X., 2015. Multiparameter adjoint tomography of the crust and upper mantle beneath East Asia: 1. Model construction and comparisons, *J. geophys. Res.,* **120,** 1762–1786.

Chen, P., Zhao, L. & Jordan, T., 2007. Full 3D tomography for the crustal structure of the Los Angeles region, *Bull. seism. Soc. Am.,* **97,** 1094–1120.

Coney, P. & Reynolds, S., 1977. Cordilleran Benioff zones, *Nature,* **270,** 403–406.

Coney, P., Jones, D. & Monger, J., 1980. Cordilleran suspect terranes, *Nature,* **288,** 329–333.

Dalton, C. & Faul, U., 2010. The oceanic and cratonic upper mantle: clues from joint interpretation of global velocity and attenuation models, *Lithos,* **120,** 160–172.

Debayle, E., Kennett, B. & Priestley, K., 2005. Global azimuthal seismic anisotropy and the unique plate-motion deformation of Australia, *Nature,* **433,** 509–512.

Dziewoński, A. & Anderson, D., 1981. Preliminary reference Earth model, *Phys. Earth planet. Inter.,* **25,** S297–S356.

Dziewoński, A. & Woodhouse, J., 1983. An experiement in the systematic study of global seismicity: centroid-moment tensor solutions for 201 moderate and large earthquakes of 1981, *J. geophys. Res.,* **88,** 3247–3271.

Ekström, G., 2011. A global model of Love and Rayleigh surface wave dispersion and anisotropy, 25–200 s, *Geophys. J. Int.,* **187,** 1668–1686.

Ekström, G. & Dziewoński, A., 1998. The unique anisotropy of the Pacific upper mantle, *Nature,* **394,** 168–172.

Ekström, G., Nettles, M. & Dziewoński, A., 2012. The global CMT project 2004–2010: centroid-moment tensors for 13,017 earthquakes, *Phys. Earth planet. Inter.,* **200,** 1–9.

Fichtner, A. & Trampert, J., 2011. Hessian kernels of seismic data functionals based upon adjoint techniques, *Geophys. J. Int.,* **185,** 775–798.

Fichtner, A. & van Leeuwen, T., 2015. Resolution analysis in full waveform inversion, *J. geophys. Res.,* **120,** doi:10.1002/2015JB012106.

Fichtner, A. & Villaseñor, A., 2015. Crust and upper mantle of the western Mediterranean-constraints from full-waveform inversion, *Earth planet. Sci. Lett.,* **428,** 52–62.

Fichtner, A., Kennett, B., Igel, H. & Bunge, H., 2009. Full seismic waveform tomography for upper-mantle structure in the Australasian region using adjoint methods, *Geophys. J. Int.,* **179,** 1703–1725.

Fichtner, A., Kennett, B., Igel, H. & Bunge, H., 2010. Full waveform tomography for radially anisotropic structure: new insights into present and past states of the Australasian upper mantle, *Earth planet. Sci. Lett.,* **290,** 270–280.

Gauthier, O., Virieux, J. & Tarantola, A., 1986. Two-dimensional nonlinear inversion of seismic waveforms: numerical results, *Geophysics,* **51,** 1387–1403.

Godey, S., Deschamps, F., Trampert, J. & Snieder, R., 2004. Thermal and compositional anomalies beneath the North American continent, *J. geophys. Res.,* **109,** doi:10.1029/2002JB002263.

Goes, S. & van der Lee, S., 2002. Thermal structure of the North American uppermost mantle inferred from seismic tomography, *J. geophys. Res.,* **107,** doi:10.1029/2000JB000049.

Grand, S., 1994. Mantle shear structure beneath the Americas and surrounding oceans, *J. geophys. Res.,* **99,** 11 591–11 621.

Grand, S., van der Hilst, R. & Widiyantoro, S., 1997. Global seismic tomography: a snapshot of convection in the Earth, *GSA Today,* **7,** 1–7.

Gung, Y., Panning, M. & Romanowicz, B., 2003. Global anisotropy and the thickness of continents, *Nature,* **422,** 707–711.

Hess, H., 1964. Seismic anisotropy of the uppermost mantle under oceans, *Nature,* **203,** 629–631.

Hjörleifsdóttir, V. & Ekström, G., 2010. Effects of three-dimensional Earth structure on CMT earthquake parameters, *Phys. Earth planet. Inter.,* **179,** 178–190.

Hoffman, P., 1988. United plates of America, the birth of a craton: Early Proterozoic assembly and growth of Laurentia, *Annu. Rev. Earth Planet. Sci,* **16,** 543–603.

Huang, H., Yao, H. & van der Hilst, R., 2010. Radial anisotropy in the crust of SE Tibet and SW China from ambient noise interferometry, *Geophys. Res. Lett.,* **37,** doi:10.1029/2010GL044981.

Jackson, D., 1972. Interpretation of inaccurate, insufficient, inconsistent data, *Geophys. J. R. astr. Soc.,* **28,** 97–109.

Jackson, I. & Faul, U., 2010. Grainsize-sensitive viscoelastic relaxation in olivine: Towards a robust laboratory-based model for seismological application, *Phys. Earth planet. Inter.,* **183,** 151–163.

Jung, H. & Karato, S., 2001. Water-induced fabric transitions in olivine, *Science,* **293,** 1460–1463.

Komatitsch, D. & Tromp, J., 1999. Introduction to the spectral-element method for 3-D seismic wave propagation, *Geophys. J. Int.,* **139,** 806–822.

Komatitsch, D. & Tromp, J., 2002a. Spectral-element simulations of global seismic wave propagation – I. Validation, *Geophys. J. Int.,* **149,** 390–412.

Komatitsch, D. & Tromp, J., 2002b. Spectral-element simulations of global seismic wave propagation – II. Three-dimensional models, oceans, rotation and self-gravitation, *Geophys. J. Int.,* **150,** 308–318.

Komatitsch, D., Xie, Z., Bozdağ, E., de Andrade, E. S., Peter, D., Liu, Q. & Tromp, J., 2016. Anelastic sensitivity kernels with parsimonious storage for full waveform inversion and adjoint tomography, *Geophys. J. Int.,* **206,** 1467–1478.

Kustowski, B., Ekström, G. & Dziewoński, A., 2008. Anisotropic shear-wave velocity structure of the Earth's mantle: a global model, *J. geophys. Res.,* **113,** B06306, doi:10.1029/2007JB005169.

Lailly, P., 1983. The seismic inverse problem as a sequence of before stack migration, in *Conference on Inverse Scattering: Theory and Application,* pp. 206–220, ed. Bednar, J., *SIAM*.

Langston, C., 2007a. Spatial gradient analysis for linear seismic arrays, *Bull. seism. Soc. Am.,* **97,** 265–280.

Langston, C., 2007b. Wave gradiometry in two dimensions, *Bull. seism. Soc. Am.,* **97,** 401–416.

Langston, C., 2007c. Wave gradiometry in the time domain, *Bull. seism. Soc. Am.,* **97,** 926–933.

Lekic, V., Panning, M. & Romanowicz, B., 2010. A simple method for improving crustal correction in waveform tomography, *Geophys. J. Int.,* **182,** 265–278.

Levander, A., Zelt, C. & Magnani, M., 2005. Crust and upper mantle velocity structure of the southern Rocky Mountains from the Jemez Lineament to the Cheyenne Belt, in *The Rocky Moutain Region: An Evolving Lithosphere, Geophys. Monogr. Ser.,* pp. 293–308, eds Karlstrom, K. & Keller, G., AGU.

Levander, A., Schmandt, B., Miller, M., Liu, K., Karlstrom, K., Crow, R., Lee, C.-T. & Humphreys, E., 2011. Continuing Colorado plateau uplift by delamination–style convective lithospheric downwelling, *Nature,* **472,** 461–466.

Levin, V. & Park, J., 1997. P-SH conversions in a flat-layered medium with anisotropy of arbitrary orientation, *Geophys. J. Int.,* **131,** 253–266.

Lin, F. & Ritzwoller, M., 2011. Helmholtz surface wave tomography for isotropic and azimuthally anisotropic structure, *Geophys. J. Int.,* **186,** 1104–1120.

Lin, F., Moschetti, M. & Ritzwoller, M., 2008. Surface wave tomography of the western United States from ambient seismic noise: Rayleigh and Love wave phase velocity maps, *Geophys. J. Int.,* **173,** 281–298.

Lin, F., Ritzwoller, M. & Snieder, R., 2009. Eikonal tomography: surface wave tomography by phase front tracking across a regional broad-band seismic array, *Geophys. J. Int.,* **177,** 1091–1110.

Lin, F., Ritzwoller, M., Yang, Y., Moschetti, M. & Fouch, M., 2011. Complex and variable crustal and uppermost mantle seismic anisotropy in the western United States, *Nat. Geosci.,* **4,** 55–61.

Liu, Q., Polet, J., Komatitsch, D. & Tromp, J., 2004. Spectral-element moment tensor inversions for earthquakes in southern California, *Bull. seism. Soc. Am.,* **94,** 1748–1761.

Liu, Q. & Tromp, J., 2006. Finite-frequency sensitivity kernels based upon adjoint methods, *Bull. seism. Soc. Am.,* **96,** 2383–2397.

Liu, Q. & Tromp, J., 2008. Finite-frequency sensitivity kernels for global seismic wave propagation based upon adjoint methods, *Geophys. J. Int.,* **174,** 265–286.

Liu, Q. & Gu, Y., 2012. Seismic imaging: from classical to adjiont tomography, *Tectonophysics,* **566,** 31–66.

Liu, L. & Stegman, D., 2012. Origin of Columbia river flood basalt controlled by propagating rupture of the Farallon slab, *Nature,* **482,** 386–389.

Liu, Y. & Holt, W., 2015. Wave gradiometry and its link with Helmholtz equation solutions applied to USArray in the eastern U.S., *J. geophys. Res.,* **120,** 5717–5746.

Liu, L., Spasojevic, S. & Gurnis, M., 2008. Reconstructing Farallon plate subduction beneath North America back to the late Cretaceous, *Science,* **322,** 934–938.

Liu, L., Gurnis, M., Seton, M., Saleeby, J., Muller, R. & Jackson, J., 2010. The role of oceanic plateau subduction in the Laramide orogeny, *Nat. Geosci.,* **3,** 353–357.

Long, M. & Silver, P., 2008. The subduction zone flow field from seismic anisotropy, *Science,* **319,** 315–318.

Love, A.E.H., 1927. *A Treatise on the Theory of Elasticity,* Cambridge Univ. Press.

Luo, Y., Modrak, R. & Tromp, J., 2013. Strategies in adjoint tomography, in *Handbook of Geomathematics,* 2nd edn, pp. 1–52, eds Freeden, Z.N.W. & Sonar, T., Springer.

Maggi, A., Tape, C., Chen, M., Chao, D. & Tromp, J., 2009. An automated time-window selection algorithm for seismic tomography, *Geophys. J. Int.,* **178,** 257–281.

Marone, F. & Romanowicz, B., 2007. The depth distribution of azimuthal anisotropy in the continental upper mantle, *Nature,* **447,** 198–201.

Marone, F., Gung, Y. & Romanowicz, B., 2007. Three-dimensional radial anisotropic structure of the North American upper mantle from inversion of surface waveform data, *Geophys. J. Int.,* **171,** 206–222.

Matthies, H. & Strang, G., 1979. The solution of nonlinear finite element equation, *Int. J. Numer. Methods Eng.,* **14,** 1613–1626.

Modrak, R. & Tromp, J., 2016. Seismic waveform inversion best practices: regional, global and exploration test cases, *Geophys. J. Int.,* **206,** 864–889.

Montagner, J. & Nataf, H., 1986. A simple method for inverting the azimuthal anisotropy of surface waves, *J. geophys. Res.,* **91,** 511–520.

Montagner, J. & Tanimoto, T., 1991. Global upper mantle tomography of seismic velocities and anisotropies, *J. geophys. Res.,* **96,** 20 337–20 351.

Monteiller, V., Chevrot, S., Komatitsch, D. & Wang, Y., 2015. Three-dimensional full waveform inversion of short-period teleseismic wavefields based upon the SEM-DSM hybrid method, *Geophys. J. Int.,* **202,** 811–827.

Moschetti, M., Ritzwoller, M., Lin, F. & Yang, Y., 2010. Seismic evidence for widespread western-US deep-crustal deformation caused by extension, *Nature,* **464,** 885–889.

Moulik, P. & Ekström, G., 2014. An anisotropic shear velocity model of the Earth's mantle using normal modes, body waves, surface waves and long-period waveforms, *Geophys. J. Int.,* **199,** 1713–1738.

Moulik, P. & Ekström, G., 2016. The relationships between large-scale variations in shear velocity, density, and compressional velocity in the Earth's mantle, *J. geophys. Res.,* **121,** 2737–2771.

Nettles, M. & Dziewoński, A., 2008. Radially anisotropic shear velocity structure of the upper mantle globally and beneath North America, *J. geophys. Res.,* **113,** doi:10.1029/2006JB004819.

Nicolas, A. & Christensen, I., 1987. Formation of anisotropy in upper mantle peridotites—a review, in *Composition, Structure and Dynamics of the Lithosphere-Asthenosphere System,* pp. 111–123, eds Fuchs, K. & Froidevaux, C., American Geophysical Union, Washington, DC.

Nishimura, C. & Forsyth, D., 1989. The anisotropic structure of the upper mantle in the Pacific, *Geophys. J. Int.,* **96,** 203–229.

Nocedal, J., 1980. Updating quasi-Newton matrices with limited storage, *Math. Comput.,* **35,** 773–782.

Nolet, G., 1990. Partitioned waveform inversion and two-dimensional structure under the network of autonomously recording seismographs, *J. geophys. Res.,* **95,** 8499–8512.

Obrebski, M., Allen, R., Pollitz, F. & Hung, S., 2011. Lithosphere-asthenosphere interation beneath the western United States from the joint inversion of body-wave traveltimes and surface-phase velocities, *Geophys. J. Int.,* **185,** 1003–1021.

Panning, M., Lekic, V. & Romanowicz, B., 2010. Importance of crustal corrections in the development of a new global model of radial anisotropy, *J. geophys. Res.,* **115,** B12325, doi:10.1029/2010JB007520.

Park, J. & Levin, V., 2002. Seismic anisotropy: Tracing plate dynamics in the mantle, *Science,* **296,** 485–489.

Park, J., Lindberg, C. & Vernon, F., 1987. Multitaper spectral analysis of high-frequency seismograms, *J. geophys. Res.,* **92,** 12 675–12 684.

Plessix, R., 2006. A review of the adjoint-state method for computing the gradient of a functional with geophysical applications, *Geophys. J. Int.,* **167,** 495–503.

Porritt, R., Allen, R. & Pollitz, F., 2014. Seismic imaging east of the Rocky Mountains with USAarray, *Earth planet. Sci. Lett.,* **402,** 16–25.

Ritsema, J., van Heijst, H.J. & Woodhouse, J.H., 1999. Complex shear wave velocity structure imaged beneath Africa and Iceland, *Science,* **286,** 1925–1928.

Romanowicz, B., 1979. Seismic structure of the upper mantle beneath the United States by three-dimensional inversion of body wave arrival times, *Geophys. J. R. astr. Soc,* **57,** 479–506.

Romanowicz, B., 2003. Global mantle tomography: progress status in the past 10 years, *Annu. Rev. Earth Planet. Sci.,* **31,** 303–328.

Schaeffer, A. & Lebedev, S., 2014. Imaging the North American continent using waveform inversion of global and USArray data, *Earth planet. Sci. Lett.,* **402,** 26–41.

Schmandt, B. & Humphreys, E., 2010. Complex subduction and small-scale convection revealed by body-wave tomography of the western United States upper mantle, *Earth planet. Sci. Lett.,* **297,** 435–445.

Schmandt, B. & Lin, F., 2014. P and S tomography of the mantle beneath the United States, *Geophys. Res. Lett.,* **41,** 6342–6349.

Shapiro, N., Ritzwoller, M., Molnar, P. & Levin, V., 2004. Thinning and flow of Tibetan crust constrained by seismic anisotropy, *Science,* **305,** 233–236.

Shapiro, N., Campillo, M., Stehly, L. & Ritzwoller, M., 2005. High-resolution surface-wave tomography from ambient seismic noise, *Science,* **307,** 1615–1618.

Shen, W., Ritzwoller, M. & Schulte-Pelkum, V., 2013a. A 3-D model of the crust and uppermost mantle beneath the Central and Western US by joint inversion of receiver function and surface wave dispersion, *J. geophys. Res.,* **118,** 1–15.

Shen, W., Ritzwoller, M., Schulte-Pelkum, V. & Lin, F., 2013b. Joint inversion of surface wave dispersion and receiver function: a Bayesian Monte-Carlo approach, *Geophys. J. Int.,* **192,** 807–836.

Sieminski, A., Liu, Q. Y., Trampert, J. & Tromp, J., 2007a. Finite-frequency sensitivity of body waves to anisotropy based upon adjoint methods, *Geophys. J. Int.,* **171,** 368–389.

Sieminski, A., Liu, Q.Y., Trampert, J. & Tromp, J., 2007b. Finite-frequency sensitivity of surface wave to anisotropy based upon adjoint methods, *Geophys. J. Int.,* **168,** 1153–1174.

Sigloch, K., 2011. Mantle provinces under North America from multifrequency *P* wave tomography, *Geochem. Geophys. Geosyst.,* **12,** doi:10.1029/2010GC003421.

Sigloch, K., McQuarrie, N. & Nolet, G., 2008. Two-stage subduction history under North America inferred from multiple-frequency tomography, *Nat. Geosci.,* **1,** 458–462.

Silver, P., 1996. Seismic anisotropy beneath the continents: probing the depths of geology, *Annu. Rev. Earth Planet. Sci,* **24,** 385–432.

Silver, P. & Chan, W., 1991. Shear wave splitting and subcontinental mantle deformation, *J. geophys. Res.,* **96,** 16 429–16 454.

Simmons, N., Myers, S., Johannesson, G. & Matzel, E., 2012. Llnl-g3dv3: Global *P* wave tomography model for improved regional and teleseismic travel time prediction, *J. geophys. Res.,* **117,** doi:10.1029/2012JB009525.

Simons, F., Van der Hilst, R., Montagner, J. & Zielhuis, A., 2000. Isostatic response of the Australian lithospehre: estimation of effective elastic thickness and anisotropy using multitaper spectral analysis, *J. geophys. Res.,* **105,** 19 163–19 184.

Simons, F., Van der Hilst, R., Montagner, J. & Zielhuis, A., 2002. Multimode Rayleigh wave inversion for heterogeneity and azimuthal anisotropy of the Australian upper mantle, *Geophys. J. Int.,* **151,** 738–754.

Sirgue, L. & Pratt, G., 2004. Efficient waveform inversion and imaging: A strategy for selecting temporal frequencies, *Geophysics,* **69,** 231–248.

Smith, M. & Dahlen, F., 1973. The azimuthal dependence of Love and Rayleigh wave propagation in a slightly anisotropic medium, *J. geophys. Res.,* **78,** 3321–3333.

Stacey, R., 1988. Improved transparent boundary formulations for the elastic wave equation, *Bull. seism. Soc. Am.,* **78,** 2089–2097.

Tape, C., Liu, Q., Maggi, A. & Tromp, J., 2009. Adjoint tomography of the southern California crust, *Science,* **325,** 988–992.

Tape, C., Liu, Q., Maggi, A. & Tromp, J., 2010. Seismic tomography of the southern California crust based on spectral-element and adjoint methods, *Geophys. J. Int.,* **180,** 433–462.

Tarantola, A., 1984. Inversion of seismic reflection data in the acoustic approximation, *Geophysics,* **49,** 1259–1266.

Tarantola, A., 2005. *Inverse Problem Theory and Method for Model Parameter Estimation,* SIAM.

Tauzin, B., van der Hilst, R.D., Wittlinger, G. & Ricard, Y., 2013. Multiple transition zone seismic discontinuities and low velocity layers below western United States, *J. geophys. Res.,* **118**(5), 2307–2322.

Tauzin, B., Bodin, T., Debayle, E., Perrillat, J.-P. & Reynard, B., 2016. Multi-mode conversion imaging of the subducted Gorda and Juan de Fuca plates below the North American continent, *Earth planet. Sci. Lett.,* **440,** 135–146.

Thomsen, L., 1986. Weak elastic anisotropy, *Geophysics,* **51,** 1954–1966.

Tian, Y., Zhou, Y., Sigloch, K., Nolet, G. & Laske, G., 2011. Structure of North American mantle constrained by simultaneous inversion of multiple-frequency *SH, SS* and Love waves, *J. geophys. Res.,* **116,** doi:10.1029/2010JB007704.

Trampert, J. & Van Heijst, H., 2002. Global azimuthal anisotropy in the transition zone, *Science,* **296,** 1297–1299.

Tromp, J., Tape, C. & Liu, Q.Y., 2005. Seismic tomography, adjoint methods, time reversal and banana-doughnut kernels, *Geophys. J. Int.,* **160,** 195–216.

Tromp, J. *et al.*, 2010. Near real-time simulations of global CMT earthquakes, *Geophys. J. Int.,* **183,** 381–389.

van der Hilst, R., Engdahl, R., Spakman, W. & Nolet, G., 1991. Tomographic imaging of subducted lithosphere below northwest Pacific island arcs, *Nature,* **353,** 37–43.

van der Hilst, R., Widiyantoro, S. & Engdahl, E.R., 1997. Evidence for deep mantle circulation from global tomography, *Nature,* **386,** 578–584.

van der Lee, S., 2002. High-resolution estimates of lithospheric thickness from Missouri to Massachustetts, USA, *Earth planet. Sci. Lett,* **203,** 15–23.

van der Lee, S. & Frederiksen, A., 2005. Surface wave tomography applied to the North American upper mantle, in *Seismic Earth: Array Analysis of Broadband Seismograms, AGU Monograph,* pp. 67–80, eds Levander, A. & Nolet, G., AGU.

van der Lee, S. & Nolet, G., 1997a. Seismic image of the subducted trailing fragments of the Farallon plate, *Nature,* **386,** 266–269.

van der Lee, S. & Nolet, G., 1997b. Upper mantle S velocity structure of North America, *J. geophys. Res.,* **102,** 22 815–22 838.

Vinnik, L., Makeyeva, L., Milev, A. & Usenko, A., 1992. Global patterns of azimuthal anisotropy and deformations in the continental mantle, *Geophys. J. Int.,* **111,** 433–447.

Virieux, J. & Operto, S., 2009. An overview of full-waveform inversion in exploration geophysics, *Geophysics,* **74,** WCC1–WCC26.

Wang, Y. *et al.*, 2016. The deep roots of the wester Pyrenees revealed by full waveform inversion of teleseismic *P* waves, *Geology,* **44,** 475–478.

West, J., Fouch, M., Roth, J. & Elkins-Tanton, L., 2009. Vertical mantle flow associated with a lithospheric drip beneath the Great Basin, *Nat. Geosci.,* **2,** 439–444.

Whitmeyer, S. & Karlstrom, K., 2007. Tectonic model for the Proterozoic growth of North America, *Geosphere,* **3,** 220–259.
Woodhouse, J. & Dziewoński, A., 1984. Mapping the upper mantle: three-dimensional modeling of Earth structure by inversion of seismic waveforms, *J. geophys. Res.,* **89,** 5953–5986.
Wortel, M.J.R. & Spakman, W., 2000. Subduction and slab detachment in the Mediterranean-Carpathian region, *Science,* **290,** 1910–1917.
Yuan, H. & Dueker, K., 2005. Upper mantle tomographic Vp and Vs images of the Rocky Moutains in Wyoming, Colorado and New Mexico: evidence for a thick hterogeneous chemical lithosphere, in *The Rocky Moutain Region: An Evolving Lithosphere, Geophys. Monogr. Ser.,* pp. 329–346, eds Karlstrom, K.E. & Keller, G.R., AGU.
Yuan, H. & Romanowicz, B., 2010. Lithospheric layering in the North American craton, *Nature,* **466,** 1063–1068.
Yuan, H., Romanowicz, B., Fischer, K. & Abt, D., 2011. 3-D shear wave radially and azimuthally anisotropic velocity model of the North American upper mantle, *Geophys. J. Int.,* **184,** 1237–1260.
Yuan, H., French, S., Cupillard, P. & Romanowicz, B., 2014. Lithospheric expression of geological units in central and eastern North America from full waveform tomography, *Earth planet. Sci. Lett.,* **402,** 176–186.
Zhang, S. & Karato, S., 1995. Lattice preferred orientation of olivine aggregates deformed in simple shear, *Nature,* **375,** 774–777.
Zhou, Y., Dahlen, F. & Nolet, G., 2004. Three-dimensional sensitivity kernels for surface wave observables, *Geophys. J. Int.,* **158,** 142–168.
Zhu, H. & Fomel, S., 2016. Building good starting models for full waveform inversion based on adaptive matching filtering misfit, *Geophysics,* **81,** U61–U72.
Zhu, H. & Tromp, J., 2013. Mapping tectonic deformation in the crust and upper mantle beneath Europe and the North Atlantic Ocean, *Science,* **341,** 871–875.
Zhu, H., Bozdag, E., Peter, D. & Tromp, J., 2012. Structure of the European upper mantle revealed by adjoint tomography, *Nat. Geosci.,* **5,** 493–498.
Zhu, H., Bozdag, E., Duffy, T. & Tromp, J., 2013. Seismic attenuation beneath Europe and the North Atlantic: implicitions for water in the mantle, *Earth planet. Sci. Lett.,* **381,** 1–11.
Zhu, H., Bozdag, E. & Tromp, J., 2015. Seismic structure of the European upper mantle based on adjoint tomography, *Geophys. J. Int.,* **201,** 18–52.
Zhu, H., Li, S., Fomel, S., Stadler, G. & Ghattas, O., 2016. A Bayesian approach to estimate uncertainty for full waveform inversion using a priori information from depth migration, *Geophysics,* **81,** R307–R323.

SUPPORTING INFORMATION

Supplementary data are available at *GJI* online.

Figure S1. Relative perturbations in isotropic shear wavespeed $\delta \ln \beta$ (left) and radially anisotropic parameter ξ(right) for the starting model US00 at depths ranging from 50 km to 300 km.
Figure S2. Horizontal cross sections of relative perturbations in isotropic compressional wavespeed for US_{22} at depths ranging from 80 km to 800 km. 1-D reference model STW105 (Kustowski *et al.* 2008) is used to compute the relative perturbations.
Figure S3. Map views and zoom in vertical cross sections (0–400 km) of relative perturbations in isotropic shear wavespeed in US_{22} for the western US. The left panel shows map views and locations of seven vertical cross sections. The right panel shows these sections.
Figure S4. Same as Fig. 3 but for the eastern US.
Figure S5. Four vertical cross sections of US_{22} across the US.
Figure S6. PSF test at 70 km beneath the western US. From left to right are input perturbation for β_v, PSF for β_v and PSF for β_h, respectively.
Figure S7. Number of measurements for bandpass filters of 25–100 s and 25–150 s, respectively.
Figure S8. Comparisons of three-component seismograms for bandpass filters of 25–100 s and 25–150 s. Panels (a) and (b) are results for 25–100 s and 25–150 s, respectively. From top to bottom are seismograms at radial, transverse and vertical components.